

# Mesoscale properties of biomolecular condensates emerging from protein chain dynamics

Nicola Galvanetto<sup>1,2†</sup>, Miloš T. Ivanović<sup>1†</sup>, Simone A. Del Grosso<sup>1</sup>, Aritra Chowdhury<sup>1</sup>, Andrea Sottini<sup>1</sup>, Daniel Nettels<sup>1</sup>, Robert B. Best<sup>3†</sup> and Benjamin Schuler<sup>1,2†</sup>

<sup>1</sup>Department of Biochemistry, University of Zurich, Zurich, Switzerland

<sup>2</sup>Department of Physics, University of Zurich, Zurich, Switzerland

<sup>3</sup>Laboratory of Chemical Physics, National Institute of Diabetes and Digestive and Kidney Diseases, National Institutes of Health, Bethesda, MD, USA

†Corresponding authors: N. Galvanetto ([n.galvanetto@bioc.uzh.ch](mailto:n.galvanetto@bioc.uzh.ch)), M. T. Ivanović ([m.ivanovic@bioc.uzh.ch](mailto:m.ivanovic@bioc.uzh.ch)), R. B. Best ([robert.best2@nih.gov](mailto:robert.best2@nih.gov)), B. Schuler ([schuler@bioc.uzh.ch](mailto:schuler@bioc.uzh.ch))

## Abstract

Biomolecular condensates form by phase separation of biological polymers and have important functions in the cell — functions that are inherently connected to their physical properties. A remarkable aspect of such condensates is that their viscoelastic properties can vary by orders of magnitude, but it has remained unclear how these pronounced differences are rooted in the nanoscale dynamics at the molecular level. Here we investigate a series of condensates formed by complex coacervation that span about two orders of magnitude in molecular dynamics, diffusivity, and viscosity. We find that the nanoscale chain dynamics on the nano- to microsecond timescale can be accurately related to both translational diffusion and mesoscale condensate viscosity by analytical relations from polymer physics. Atomistic simulations reveal that the observed differences in friction — a key quantity underlying these relations — are caused by differences in inter-residue contact lifetimes, leading to the vastly different dynamics among the condensates. The rapid exchange of inter-residue contacts we observe may be a general mechanism for preventing dynamic arrest in compartments densely packed with polyelectrolytes, such as the cell nucleus.

## Introduction

A substantial fraction of all cellular proteins (1) are organized in biomolecular condensates formed as a consequence of phase separation, an intriguing and important feature of subcellular organization (2–4). The role of these membraneless bodies in regulating cellular homeostasis is central, as they coordinate numerous biological functions by means of the assembly of proteins and nucleic acids (5–7). The underlying cellular processes span a wide spectrum of time- and length-scales (8), they are governed by the physical properties of the condensates (9) and the molecular driving forces that lead to phase separation (10–12). At the molecular scale, the rate at which biomolecules explore different conformations determines the efficiency of biochemical interactions and reactions (13, 14). These processes and their spatial organization are controlled by the translational diffusion of biomolecules within phase-separated organelles as well as the biomolecular exchange with the external environment (15–17). At the mesoscopic scale, material properties play a role; for example, bulk viscosity affects the fusion times of condensates (18), which can influence cell fate (19, 20). This multi-scale complexity poses a considerable challenge in deciphering the relationships between these dynamic processes and establishing quantitative relations that can predict and explain the behavior of biomolecular condensates. The nanoscale dynamics of biomolecular conformations are expected to be related to translational diffusion (21) and to the emergent bulk viscosity of the percolated network they form (22). Material properties ultimately derive from the interaction strengths among the biomolecules that drive phase separation, and therefore from their specific amino acid sequences (23–29), but how molecular and mesoscale dynamics are linked quantitatively is an open question.

A biological example with this multi-scale complexity is the cell nucleus (7, 30, 31) which is rich in highly charged biomolecules. To compensate for the high negative net charge

of DNA, highly positively charged proteins, such as histones and protamines, have evolved to compact the chromosomes (32). Other highly charged intrinsically disordered proteins (IDPs) are involved in remodeling chromatin and regulating gene expression and replication. For instance, the negatively charged prothymosin  $\alpha$  (ProT $\alpha$ ) can sequester histone H1 and accelerate its dissociation from nucleosomes (33–35). The two oppositely charged disordered proteins histone H1 and ProT $\alpha$  form viscous droplets by complex coacervation at near-physiological salt concentrations, but maintain surprisingly rapid dynamics at the molecular level (36). However, viscosities and chain dynamics are expected to depend on the chemical nature of these biological polyelectrolytes and the solution conditions, especially the salt concentration. Here we aim to identify general relations between the molecular and mesoscopic properties of biomolecular condensates across a wide range of dynamics.

We focus on complex coacervates between highly charged intrinsically disordered proteins and peptides. In the condensates they form, associative phase separation is driven by electrostatic interactions (37, 38) and is thus highly sensitive to salt concentration and the identity of the charged residues (39, 40). We employ a combination of single-molecule techniques to investigate the conformational dynamics of the polypeptides, and microrheology to assess mesoscale properties. We find that the chain dynamics of intrinsically disordered proteins within these condensates range from hundreds of nanoseconds to tens of microseconds. These reconfiguration times correlate linearly with the translational diffusion coefficients of the proteins and the bulk viscosity of the condensates. From large-scale all-atom molecular dynamics (MD) simulations, we find that low salt concentrations and especially the presence of arginine residues increase the lifetimes of inter-chain contacts, which slows down larger-scale condensate dynamics. Altogether, we thus demonstrate a direct relation between the nanoscopic dynamics of protein

reconfiguration, mesoscale translational motion, and macroscopic viscosity within biomolecular condensates. These relations can be rationalized within the framework of semidilute

polymer solutions and generalized to predict the behavior of condensates across scales.

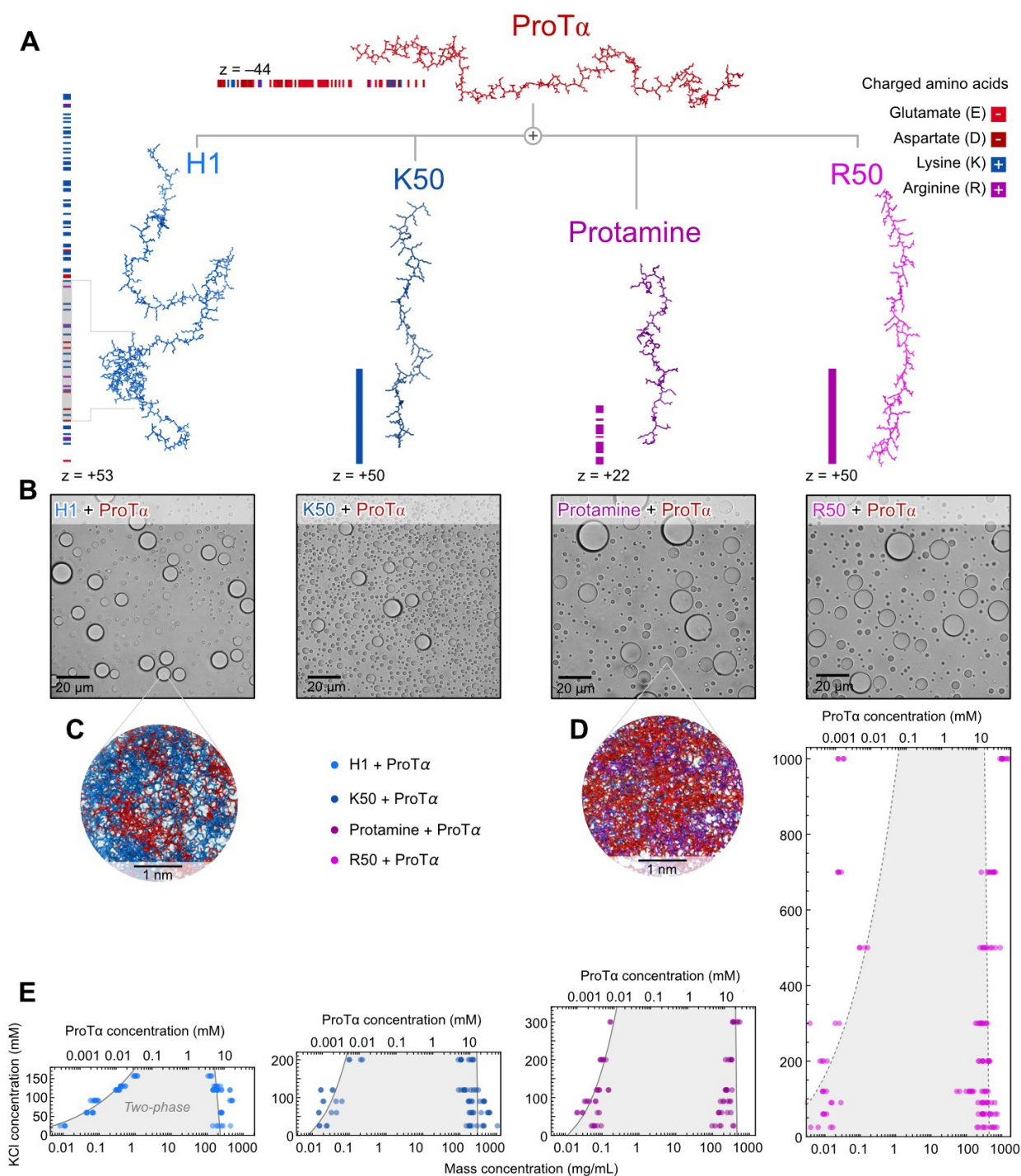


**Figure 1. Phase separation of charged polypeptides strongly depends on their amino acid sequences.** (A) Illustration of polymers used in this study with the distribution of charges along their sequences, and net charges ( $z$ ): ProT $\alpha$ , protamine, and H1 are naturally occurring polycationic proteins; poly-L-arginine-50 (R50) and poly-L-lysine-50 (K50) are synthetic polycations (Supplementary Table 1). The gray band in the H1 sequence indicates the globular domain. (B) Brightfield microscopy images of phase-separated samples of ProT $\alpha$  mixed with a polycation (protamine, H1, R50, or K50) at charge balance in TEK buffer at 90 mM KCl (ionic strength 98 mM). Scale bar, 20  $\mu$ m. (C) Illustration of the polymer networks on the nanoscale in the dense phases of H1 + ProT $\alpha$  and (D) protamine + ProT $\alpha$  from molecular dynamics simulations. (E) Phase diagrams from coexistence measurements of dense and dilute phases as a function of salt concentration. The total mass concentration of both components (bottom axis) is based on the measured ProT $\alpha$  concentrations (top axis) and the charge-balanced ratio at which ProT $\alpha$  and the positive partner were mixed (36) (ProT $\alpha$ :H1 1.2:1, ProT $\alpha$ :K50 1.13:1, ProT $\alpha$ :protamine 0.5:1, ProT $\alpha$ :R50 1.13:1, see Supplementary Fig. 1). Phenomenological fit with a binodal curve based on Voorn–Overbeek theory (41) (solid line, dashed for ProT $\alpha$ :R50 where the theory fails to capture the complex interactions of arginine beyond electrostatics (42, 43)).

## Results

### Phase separation of biological polyelectrolytes

To be able to assess the influence of amino acid sequence and composition, we used the highly negatively charged disordered protein ProT $\alpha$  in combination with four positively charged polypeptides with different charge densities and amino acid composition (Figure 1A): the natural IDPs histone H1 (net charge +53) and protamine (net charge +22), and two disordered homopolypeptides with 50 lysine (K50) or arginine (R50) residues, respectively (both net charge +50). The strong electrostatic interactions between ProT $\alpha$  and each of the four positively charged partners leads to associative phase separation when mixed at charge-balanced stoichiometries (Supplementary Fig. 1), as expected for oppositely charged polyelectrolytes (44, 45). Viewed under a light microscope, all phase-separated samples appear visually indistinguishable, with an aqueous dilute phase and spherical droplets of dense phase (Figure 1B–D). For all of them, the dense phase has a total protein mass concentration above 100 mg/mL. However, phase separation of the four samples responds differently to the salt concentration: At an initial protein concentration of  $\sim 10 \mu\text{M}$ , phase separation is difficult to achieve above 200 mM KCl for the lysine-rich polypeptides, but the arginine-rich polypeptides readily phase-separate with ProT $\alpha$  at higher salt — for R50 even above 1 M KCl. This observation and the corresponding phase diagrams (Figure 1E) highlight quantitative differences in the nature of the interactions of these two positively charged residues (40, 46–48) related to differences in their chemical structure, charge distribution, and polarizability (49). We thus asked how these different interactions affect the conformations and dynamics of the polypeptides that make up the condensates, as well as the corresponding mesoscopic properties.

### Condensate dynamics across scales

To probe the conformations and intrachain dynamics of individual proteins within the different dense phases at the nanoscale, we used confocal single-molecule Förster resonance energy transfer (FRET) spectroscopy. We prepared droplets with unlabeled samples and doped them with ProT $\alpha$  double-labeled with Cy3B as a donor and CF660R as an acceptor at positions 56 and 110. The doping ratio between labeled and unlabeled protein was adjusted to yield final concentration of  $\sim 100 \text{ pM}$  labeled ProT $\alpha$  within the droplets to enable FRET measurements with single-molecule resolution (Figure 2A, B). The resulting FRET efficiency histograms show that free monomeric ProT $\alpha$  in dilute solution is expanded at low salt concentration, resulting in a low mean transfer efficiency,  $\langle E \rangle$ , due to the repulsion between the negative charges along the chain, which are screened at high salt, leading to chain compaction (50, 51) (see Figure 2 C, D). The higher FRET efficiencies of ProT $\alpha$  inside the condensate droplets indicate chain compaction, which increases with the charge density and the arginine content of the polycationic interaction partners, resulting in stronger interactions with ProT $\alpha$  (Figure 2C). In contrast to the free monomeric chain, ProT $\alpha$  within the droplets experiences a slight expansion with increasing salt concentration, reflected by a decrease in  $\langle E \rangle$  (Figure 2D). Since we observe no significant correlation between protein mass concentration and chain dimensions (Supplementary Fig. 2A), the most likely cause of this expansion is the screening of the electrostatic attraction between oppositely charged chains by salt.

The intrinsically disordered protein ProT $\alpha$  samples a heterogeneous ensemble of conformations within the droplets (36). We measured the corresponding chain relaxation (22) or reconfiguration times,  $\tau_r$ , by monitoring the fluctuations of the acceptor-donor distance using single-molecule FRET combined with nanosecond fluorescence correlation spectroscopy (nsFCS) (52, 53) (Figure 2E, F, see Methods). The chain dynamics of ProT $\alpha$  in the dense phases are highly dependent on the identity of the polycationic partner. ProT $\alpha$  and the lysine-rich H1 form droplets in which the protein rearrangements are extremely fast, with  $\tau_r$  of hundreds of nanoseconds (36), whereas in arginine-rich droplets, chain reconfiguration is slowed down by more than an order of magnitude, with  $\tau_r$  exceeding  $10 \mu\text{s}$  (Figure 2F, G). In addition to the dependence on sequence composition,  $\tau_r$  in the droplets exhibits a trend with increasing salt concentration and decreases by a factor of 2 to 3 over the salt concentrations accessible for the different condensates (Figure 2G). This observation is consistent with the hypothesis that ions screen the intermolecular interactions that slow down chain rearrangements, as reflected by the moderate chain expansion at high salt concentration (Figure 2D).

From the FCS measurements (Figure 2E), we can also extract the diffusion time,  $\tau_D$ , of the labeled protein molecules through the confocal volume (Figure 2H, see Methods). While  $\tau_r$  reports on the nanoscopic dynamics within the polypeptide chain,  $\tau_D$  provides information on the translational motion of the protein through the percolated network of the condensate on the micrometer length scale of the confocal volume and is inversely proportional to the diffusion coefficient. The dependence of the translational diffusion of ProT $\alpha$  on the sequence composition of the binding partner and the salt concentration shows remarkably similar trends as the nanoscopic chain dynamics (compare Figure 2H and G): ProT $\alpha$  diffuses more rapidly in droplets with lysine-rich than with arginine-rich interaction partners and at high salt than at low salt concentrations.

To characterize the mesoscopic dynamics of the condensates, we used microrheology and monitored the diffusion of fluorescent beads inside the droplets by tracking fluorescent beads of 100 and 500 nm diameter (Supplementary Fig. 3A, B). From the mean squared displacement, we obtained the viscosity from the Stokes–Einstein relation (Methods). Viscosity is a length-scale dependent quantity in condensates (36, 54), but in this study we focus on the bulk viscosity by using beads much larger than the correlation lengths of the protein networks (22) (Methods). The viscosity in the droplets is remarkably different for the complex coacervates with different polycationic proteins and ranges from  $\sim 300$  to  $\sim 10,000$  times the viscosity of water (Figure 2I). These values remain constant for days in a given sample, indicating the absence of aging effects over this period.

In summary, the salt concentration and especially the amino acid sequence composition have a strong influence on the dynamic properties of the condensates across length- and timescales, from the nanoscopic chain reconfiguration time to the microscopic translational diffusion time of molecules and the viscosity at the mesoscopic scale of entire droplets (Figure 2G–I). The changes span nearly two orders of magnitude for each of the physical properties studied, with remarkably high correlations between them (Figure 2J), suggesting an underlying causal link across scales. To identify the molecular origins of the experimentally observed behavior, we turned to large-scale molecular dynamics (MD) simulations.





curves with linear time binning in the range where chain dynamics dominate the signal. (G) ProT $\alpha$  reconfiguration time,  $\tau_r$ , in the different coacervates as a function of salt concentration obtained from the FCS fits as shown in E/F (see Methods). Error bars, standard deviations calculated from three measurements or the error of the fit of  $\tau_r$ , whichever was greater (see Methods). (H) Translational diffusion time of double-labelled ProT $\alpha$  in the different coacervates as a function of salt concentration obtained from the FCS fits as shown in E (see Methods). Error bars, standard deviation of  $n \geq 3$  measurements. (I) Viscosity from measurements of translational diffusion of 100- and 500-nm polystyrene beads within the different coacervates from particle tracking (see Methods) as a function of salt concentration. Error bars, standard deviation of  $n \geq 20$  tracked beads. (J) Correlations between the data in G, H and I indicate a physical relation between condensate dynamics across length scales.

### Interaction dynamics from atomistic simulations

We used large-scale all-atom MD simulations with explicit solvent in a recently validated (36) slab configuration (55) (see Methods) to investigate the experimentally observed trends at the atomistic level. To assess the role of lysine versus arginine, we simulated systems consisting of 96 ProT $\alpha$  and 80 H1 molecules in one case, and 96 ProT $\alpha$  and 197 protamine molecules in the other. The two systems correspond to roughly 4 and 2.6 million atoms in the simulation box, respectively (Figure 3A, B, Supplementary Videos 1 [\[link\]](#) and 2 [\[link\]](#)). To study the effect of salt concentration, we performed simulations with 8 mM and 128 mM KCl for both systems.

The previous in-depth comparison of the simulations for ProT $\alpha$  and H1 with experimental observables, including protein concentrations, translational diffusion coefficients, intrachain distances, and chain dynamics, provided a validation of simulations with the force field and slab configuration employed (36). Moreover, the simulations at lower salt concentration and with protamine instead of H1 reproduce the higher protein concentrations (Supplementary Fig. 4) and the slower chain dynamics observed experimentally in droplets (Figure 3C, Supplementary Fig. 5), indicating that the force field also captures the differences in amino acid-specific interactions (27).

On average, each ProT $\alpha$  molecule in the dense phase is simultaneously in contact with  $\sim 6$ -7 H1 or  $\sim 11$  protamine molecules, respectively, at any given time (Figure 3D). Information on the distribution of interactions between positively and negatively charged side chains in the resulting percolated network (56) can be obtained from contact profiles (Figure 3E) and contact maps (Supplementary Fig. 6). The average number of contacts that each residue in ProT $\alpha$  makes with other chains reveals remarkably similar interaction patterns in the dense phases with the different interaction partners, with local maxima at clusters of negatively charged residues in ProT $\alpha$  (36, 57). The absolute numbers of contacts, however, differ substantially between the different dense phases: The average number of contacts ProT $\alpha$  residues make with protamine is  $\sim 80\%$  greater than with H1, and  $\sim 10\%$  greater at 8 mM than at 128 mM salt. The origin of the pronounced difference in interaction strength between lysine- and arginine-rich sequences in the simulations is expected to lie in the characteristic multipole of arginine (58), its weak hydration (59), and large polarizability (49), although especially the latter can only be captured indirectly with non-polarizable force fields (60).

Therefore, the stronger interchain interactions at low salt and for arginine-rich sequences are likely to be at the root of the slower dynamics observed experimentally (Figure 2). Indeed, the average lifetime of contacts in the dense-phase simulations of protamine-ProT $\alpha$  is about 10 times longer than for H1-ProT $\alpha$  (Figure 3F). The duration of the contacts is in turn expected to be a determining factor for the motion of the polypeptide chain as a whole (26, 28, 61, 62). This expectation is corroborated by the remarkable correlation between contact lifetimes and the chain reconfiguration times estimated from the simulations (Figure 3G) (see Methods for details). The similarity

between simulated and measured reconfiguration times (Figure 3C) further suggests that the atomistic picture emerging from the MD simulations can help to explain the dynamics observed experimentally.

The simulations yield a picture in which charged residues form close contacts, as reflected by a pronounced short-range peak in the residue-residue distance distribution that is absent for uncharged residues (Figure 3H). This sticker-like interaction (63, 64) is also reflected in the diffusion profile of charged residues, which at short times show a lower mobility than their uncharged neighbors. However, these differences average out at longer times when the motion is dominated by larger chain segments (Figure 3I). It is worth noting that the contact lifetimes between individual charged residues are roughly two orders of magnitude shorter than the reconfiguration times of the polypeptide chains. An important contribution to the short lifetimes of contacts is the rapid exchange between interacting side chains at the exceedingly high concentrations of charged residues in the molar range within the dense phases (36) (Figure 3J, K). Owing to the separation of timescales between contact lifetimes and the reconfiguration dynamics of entire chains, tens of thousands of residue-residue contacts are made and broken during  $\tau_r$  (Figure 3F). Correspondingly, the differences in the strength of side chain interactions of lysine and arginine can also be considered to result in differences in the average frictional forces acting on the chains.

### Universal link between nanoscale and mesoscale dynamics in condensates

The effects of amino acid composition and salt concentration observed in the simulations, and the correlation of contact lifetimes with reconfiguration times imply a quantitative link between side chain interactions and larger-scale motion (Figure 3G), as previously suggested based on coarse-grained simulations (26, 28, 29, 61, 62). Striking linear correlations are also observed between the experimental chain reconfiguration times, translational diffusion times, and droplet viscosity (Figure 2J). Given these correlations across length- and timescales, we thus seek a physical model for condensate dynamics that allows us to predict mesoscale properties from the nanoscale dynamics.

Polymer physics presents an opportunity to conceptualize the dynamics of biomolecules in condensates across scales (Figure 4A-C). The nature of the residue-residue interactions observed in the simulation are suggestive of a model that considers the effect of stickers explicitly. However, established quantitative models assume the lifetime of the crosslinks to be longer than chain dynamics (63, 65), which is not the case here. In fact, we are closer to the opposite limit: the contact lifetimes are orders of magnitude shorter than chain reconfiguration times, so that thousands of contacts are made and broken along the chain during  $\tau_r$  (Figure 3F). The effect of side chain interactions on the timescale of  $\tau_r$  may thus better be represented in terms of an overall drag captured by a friction coefficient. This idea is used in the Rouse model of polymer solutions (Figure 4B) (21, 22, 66), which describes the



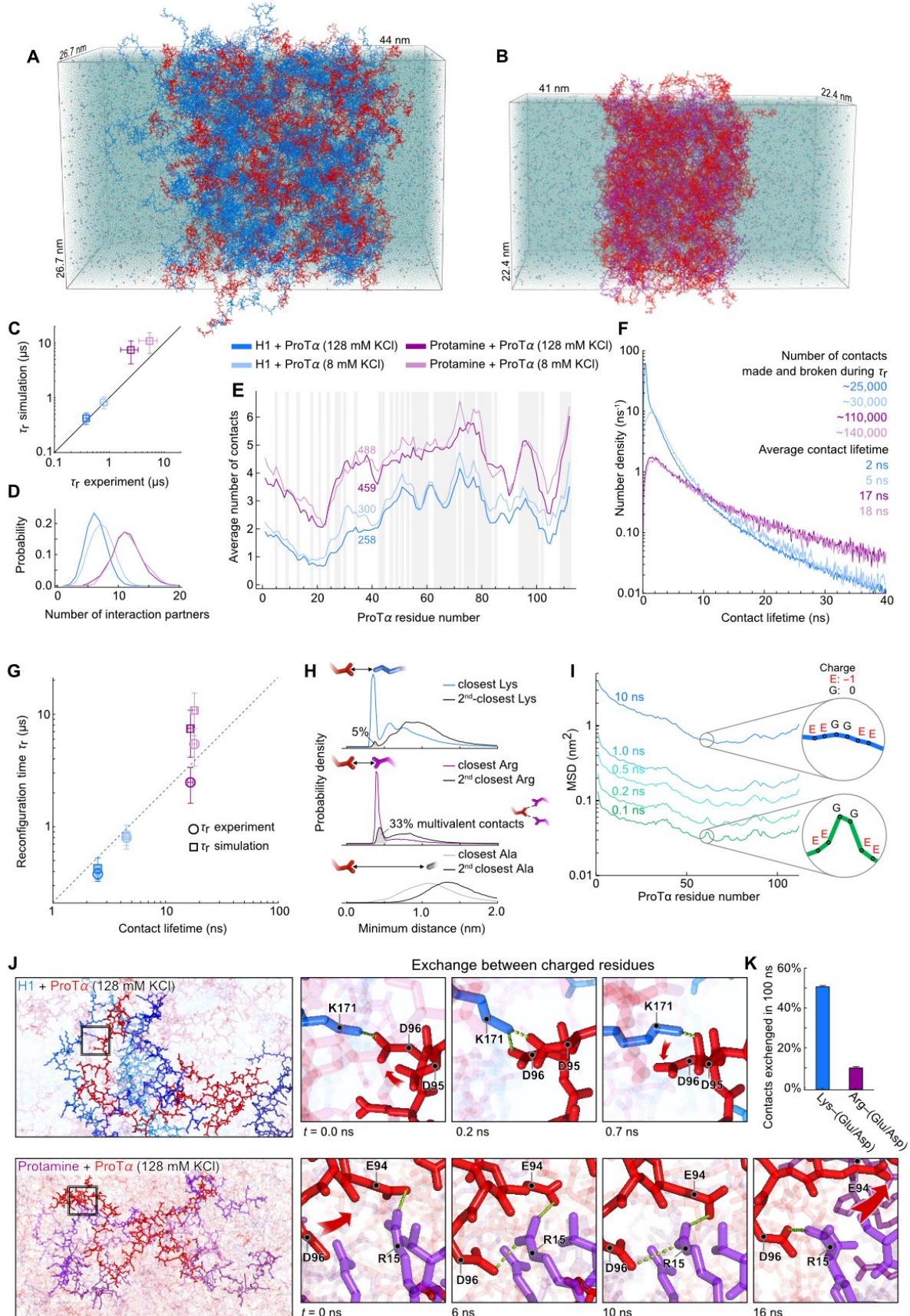


**Figure 3. All-atom simulations of dense phases at different salt concentrations.**

(A) All-atom explicit-solvent simulations of 96 ProTα (red) and 80 H1 molecules (blue) and (B) for 96 ProTα (red) and 197 protamine molecules (purple) in slab geometry<sup>55</sup>, including water (transparent blue spheres),  $\text{K}^+$  ions (blue spheres), and  $\text{Cl}^-$  ions (red spheres). (C) Comparison between the experimental chain reconfiguration time,  $\tau_r$ , and the corresponding distance decorrelation time between residues 58 and 112 (corresponding to the dye positions) from simulations ( $\tau_r$  of protamine–ProTα slab at 8 mM KCl concentration is compared with the value measured at 25 mM KCl due to experimental limitations in performing stable single-molecule recordings at low salt conditions; for uncertainties, see Methods). (D) Distribution of the number of H1 and protamine molecules simultaneously in

contact with a single ProTa. (E) Average number of contacts made by each residue of ProTa in the four dense phases, with the average total number of contacts indicated. Gray bands indicate negatively charged residues. (F) Distribution of the lifetimes of contacts made by ProTa in the four dense phases. The areas under the curves correspond to the total number of new contacts formed per chain in one nanosecond. We report the number of contacts made and broken by a single ProTa chain during its reconfiguration time obtained from simulations. (G) Correlation between the average contact lifetime of individual residues in the four dense phases and the chain reconfiguration time indicates the frictional nature of intermolecular contacts, which slows down chain dynamics (for uncertainties, see Methods). (H) Distance distribution of the closest and the 2<sup>nd</sup>-closest lysine (charge +1), arginine (+1) and alanine (0) to glutamate (-1) residues in ProTa chains (Lys and Ala distributions from H1-ProTa slab, Arg distributions from protamine-ProTa slab, both at 128 mM KCl). A sharp peak is present only in the distributions between oppositely charged residues. The shaded gray area represents the fraction of glutamate side chains involved in a multivalent close contact with two positively charged residues, which is 6-fold higher for arginine than for lysine (see Methods). (I) Mean-square displacement (MSD) of the individual ProTa residues at increasing lag times show that the lower friction (higher mobility) of uncharged residues resulting from weaker contacts is evident at short times, but is subsequently smoothed out at longer times when differences in friction for individual residues are averaged over longer chain segments. (J) Example of exchange between lysine salt bridges in H1-ProTa (top) and arginine salt bridges in protamine-ProTa dense phases (bottom). Multivalent contacts (67) between negatively charged residues and arginine are more frequent (H) and more stable than with lysine, as illustrated by representative snapshots from the simulations (see also Supplementary Videos 1 and 2). (K) Lysine exchanges partners more rapidly due to competition between the closest and the 2<sup>nd</sup>-closest negatively charged residue (histogram shows the fraction of Lys and Arg contacts where, within 100 ns, the 2<sup>nd</sup>-closest negatively charged residue—be it Glu or Asp—replaces the closest. See Methods).

dynamics of chains in terms of  $N$  connected segments subjected to Brownian motion and to a friction coefficient  $\zeta$ . The resulting relation between the translational diffusion coefficient of the entire chain,  $D = \frac{k_B T}{N\zeta}$ , and the chain reconfiguration (or Rouse) time,  $\tau_R$ , is

$$\tau_R = \frac{\langle R^2 \rangle}{3\pi^2 D}, \quad \text{Eq. 1}$$

where  $\langle R^2 \rangle$  is the mean squared end-to-end distance of the chain,  $T$  is the temperature, and  $k_B$  the Boltzmann constant (see Methods). The bulk droplet viscosity,  $\eta$ , can be expressed in terms of the friction coefficient  $\zeta$  acting on the individual chain segments and thus in terms of the experimental observables  $D$  and  $\tau_R$  according to

$$\eta(D) = \eta_s + \frac{k_B T c_p \langle R^2 \rangle}{36 D} \quad \text{and} \quad \text{Eq. 2}$$

$$\eta(\tau_R) = \eta_s + \frac{\pi^2 k_B T c_p}{12} \tau_R, \quad \text{Eq. 3}$$

where  $\eta_s$  is the solvent viscosity, and  $c_p$  is the protein concentration in the condensates (see Methods). Using the experimentally measured values of  $\eta$ ,  $c_p$ , and  $\tau_R$ , the model correctly predicts — without any adjustable parameters — the linear dependencies observed experimentally, with absolute values within an order of magnitude of the experimental findings (Figure 4D, dashed lines). The model thus explains much of the mesoscopic properties of the droplets based on the notion that a polymer chain within the droplet behaves essentially like an isolated polymer within a more viscous medium imparting friction on the chain segments. The MD simulations support this notion based on the separation of timescales between contact lifetimes and chain reconfiguration and the large number of contacts made and broken during the reconfiguration time. The proportionality between contact lifetimes and chain reconfiguration times (Figure 3G) is additional evidence that friction arises from the duration of individual contacts.

However, based on the measured chain dimensions and protein concentrations, with average protein volume fractions between 17% and 31% (Figure 1E and Methods), the dense phase is in the semidilute regime (see Methods), where the chains partially overlap, indicating that interactions beyond purely frictional contributions may need to be taken into account. Indeed, the entanglement concentration is estimated

to be in the range of the protein concentrations we observe in the dense phases (see Methods), suggesting that we are in a regime corresponding to the onset of entanglement between chains (68). This conclusion is supported by the MD simulations, which indicate that every protein chain interacts with 6 to 11 other chains (Figure 3D), suggesting a contribution of entanglement-like effects that restrict the reorientation of the chains within the network of other chains (66, 69, 70). Under these conditions, the experimentally observable chain reconfiguration time corresponds to the disentanglement time  $\tau_d$  (Supplementary Fig. 7B, Methods). Including entanglement in the Rouse model (Eq. 2 and 3) yields a correction to the expressions for viscosity by a factor  $\frac{\langle R^2 \rangle}{a^2}$ , i.e. (66, 71)

$$\eta(D) = \eta_s + \frac{k_B T c_p \langle R^2 \rangle}{36} \frac{\langle R^2 \rangle}{a^2} \frac{1}{D} \quad \text{and} \quad \text{Eq. 4}$$

$$\eta(\tau_d) = \eta_s + \frac{\pi^2 k_B T c_p \langle R^2 \rangle}{12} \frac{\langle R^2 \rangle}{a^2} \tau_d, \quad \text{Eq. 5}$$

which yields quantitative agreement with the experiments for all samples for an effective tube diameter (69), or entanglement spacing (71),  $a$ , of  $4 \pm 2$  nm (Figure 4D, Supplementary Fig. 7A, see Methods). The value of  $a$  is only by a factor of  $\sim 2$  smaller than the chain dimensions, indicating that the systems are only weakly entangled, as expected for such relatively short chains. Nevertheless, this contribution is essential for achieving quantitative agreement with experiment, and the same value of  $a$  describes the observed relation between viscosity and diffusion coefficient, as well as the relation between viscosity and reconfiguration time (Eq. 4 and 5, Figure 4D). It is worth emphasizing that the relation between diffusion coefficient and reconfiguration time has no adjustable parameter, and for the other relations, the only adjustable parameter,  $a$ , turns out to be of the same order as the correlation length (72) estimated from the protein concentration in the condensates (see Methods); all other parameters are defined by experimental observables (see Methods).

The agreement with the Rouse model for all coacervates we investigated raises the question of whether its applicability is limited to complex coacervates of highly charged proteins. We thus compared with the behavior of four other phase-separated systems: three proteins that form biomolecular condensates and for which diffusion coefficients and bulk viscosities have been reported,

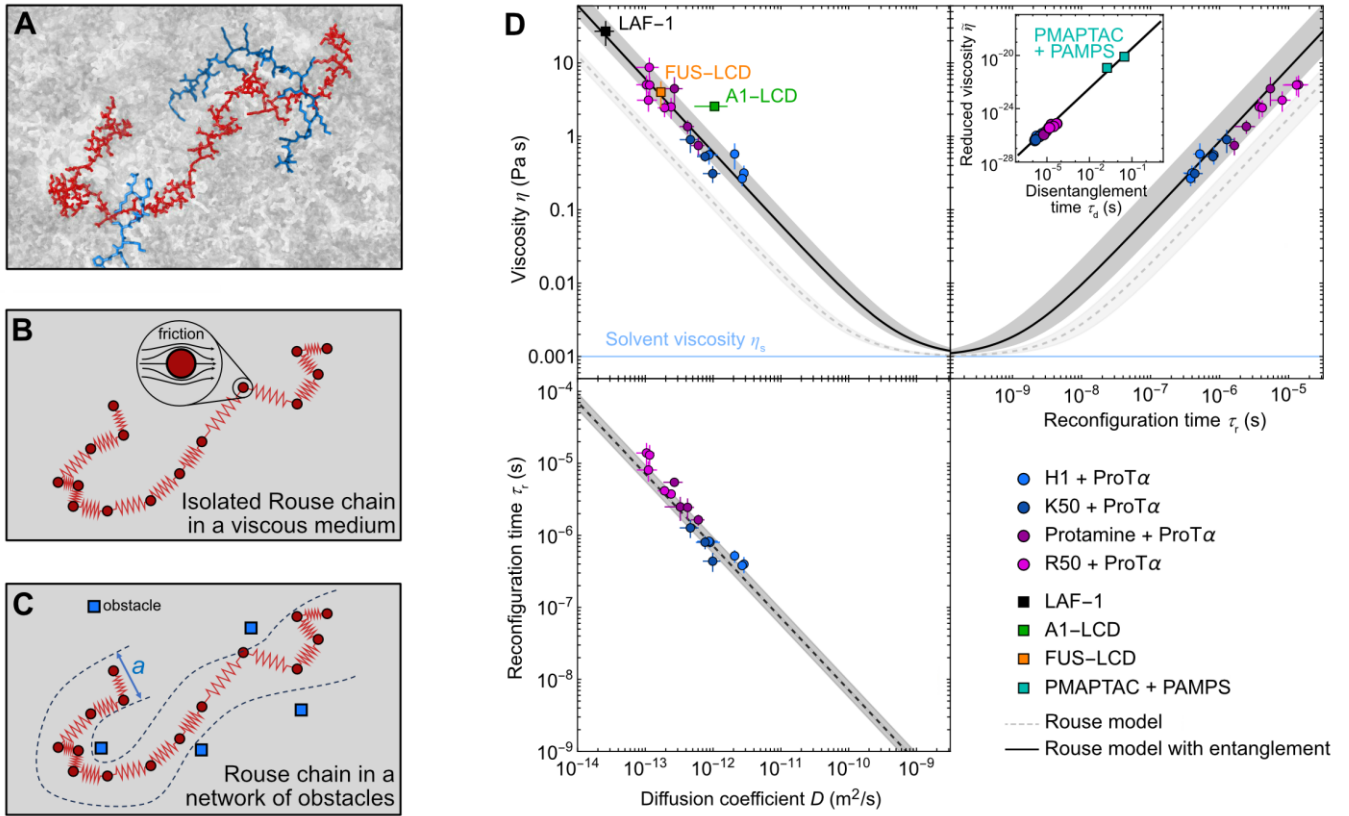


**Figure 4. Polymer models provide a link between single chain dynamics, translational diffusion, and macroscopic viscosity.** (A) Illustration of a ProTa molecule (red) in the H1-ProTa dense phase (gray) from MD simulations, with two H1 segments (blue) entangled with ProTa. (B) Schematic of the Rouse model corresponding to A, with beads (red circles) subject to Brownian motion and friction from the environment, and entropic springs connecting them. (C) Schematic of the Rouse model with entanglement, or reptation model, where the motion of a Rouse chain is constrained by a network of obstacles with a characteristic distance between them equal to  $a$ , known as the tube diameter (70) or entanglement spacing (71). (D) Comparison of the experimentally observed viscosities, diffusion coefficients, and chain reconfiguration times with the prediction of the Rouse model (dashed line) and the Rouse model with entanglement (solid line) from Equations 1-5 (see Methods), including the viscosities and diffusion coefficients of LAF-1 (54), A1-LCD (73, 74), and FUS-LCD (75, 76). The inset reports the relation in Eq. 5 between the disentanglement time,  $\tau_d$  (roughly corresponding to  $\tau_r$ , see Methods), and the reduced viscosity,  $\bar{\eta} = (\eta(\tau_d) - \eta_s)a^2 / c_p \langle R^2 \rangle$  in  $\text{Pa s m}^3$ , which allows us to compare our samples with PMAPTAC + PAMPS (chain lengths P619 and P1188) (77). The error bands of the fits account for the differences in entanglement spacing,  $a$  (Supplementary Fig. 7A), chain dimensions, and protein concentration between the different samples. Data are presented as mean values  $\pm$  s.d. (see Methods).

LAF-1 (54), A1-LCD (73, 74)<sup>a</sup> and FUS-LCD (75, 76); and one synthetic complex coacervate widely used in industrial applications, PMAPTAC (poly([3-(methacrylamido)propyl]trimethylammonium chloride)) and PAMPS (poly(2-acrylamido-2-methyl-1-propanesulfonic acid) (77), with bulk viscosities and disentanglement times<sup>b</sup> orders of magnitude above those of the biomolecular systems. Remarkably, those data are in line with the coacervates studied here (Figure 4D), suggesting that the Rouse framework we propose is more generally applicable and may provide a simple universal link between nanoscopic, microscopic, and mesoscopic behavior of biomolecular condensates formed by disordered proteins. As a result, we can provide order-of-magnitude estimates for the expected end-to-end reconfiguration times of those proteins in their dense phases: approximately 0.5–5  $\mu\text{s}$  for A1-LCD, 3–30  $\mu\text{s}$  for FUS-LCD, and 10–100  $\mu\text{s}$  for LAF-1.

<sup>a</sup> The diffusion coefficient was estimated from the radius of gyration, the diffusion time through the confocal volume, and the size of the confocal volume.

<sup>b</sup> The disentanglement time, or reptation time (22), was inferred from the crossover frequency in rheological measurements. The agreement

## Discussion

Our results demonstrate a close link between the strength of interactions at the molecular scale mediated by differences in amino acid composition and the micro- and mesoscale dynamics of biomolecular condensates. The success of the Rouse model for a range of different biomolecules, including both the complex coacervates investigated here and several homotypic condensates studied previously, indicates that the underlying physics of these systems is remarkably similar. As expected from the high protein concentrations inside the condensates, and as indicated by the MD simulations of the complex coacervates investigated here as well as previous simulations of condensates (28, 56, 78, 79), the protein chains form a highly connected network of interactions, the hallmark of viscoelastic network fluids. Despite the expected viscoelasticity of such systems, we observe the viscous component of the shear relaxation modulus to be dominant for the complex

of all data with Eq. 5 (inset in Figure 4D) highlights the consistency between FRET-based nsFCS for direct measurements of chain dynamics and the indirect determination of those dynamics from the viscoelastic properties of polymer solutions.



coacervates formed from highly charged disordered proteins on the accessible timescales, both in the present work and in our previous results on H1 and ProTα (36). For instance, the microrheological measurements by bead tracking are well described in terms of normal Brownian diffusion down to the shortest accessible timescales in the millisecond range (Supplementary Fig. 3B-D); for H1-ProTα, droplet relaxation upon fusion is single-exponential, with a relaxation time proportional to the radius of the final droplet, which also indicates that the viscoelasticity of the dense phase on the millisecond timescale and above is dominated by a viscous (rather than an elastic) component (80). The MD simulations performed for H1-ProTα (36) and protamine-ProTα (Figure 3) suggest a molecular mechanism contributing to the pronounced fluidity of these complex coacervates: The extreme concentration of charged side chains of >1 M in the dense phase, corresponding to an average distance between charged groups of <1 nm, facilitates the formation of transient ternary interactions between multiple charged groups. These interactions lead to the rapid exchange of contacts between residues on the low nanosecond timescale (Figure 3J) (36). This type of dynamic shuffling may be essential for many processes in the cell, e.g., to prevent dynamic arrest in compartments such as the cell's nucleus, which is densely packed with highly charged polyelectrolytes (31, 81).

The abundant evidence for an elastic contribution to stress relaxation in other biomolecular condensates (23, 82–84) raises the question of why viscous relaxation dominates for the coacervates we studied. To address this point, we estimated the frequency dependence of the loss and storage moduli according to Rouse theory based on our experimentally defined parameters (Supplementary Fig. 8). The resulting prediction is that the crossover frequency of the two moduli occurs in the range of the inverse chain reconfiguration time (21, 66, 72). This result implies that for the coacervates investigated here, the elastic component is expected to be dominant only on timescales in the microsecond range and below, and would thus require megahertz microrheology (85). Our observations and the relations we propose are even in agreement with measurements on synthetic coacervates whose reconfiguration times of ~1 s correspond to bulk viscosities six orders of magnitude above those of our systems (77). Therefore, biomolecular condensates with pronounced elastic relaxation at lower frequencies (23, 82–84) would thus be expected to show correspondingly slower chain reconfiguration and much higher viscosities. We note, however, that such systems are likely to be described by physics beyond simple polymer dynamics: they may form supramolecular networks with long-lasting crosslinks between molecules, and their viscoelastic moduli are thus expected to be dominated by the timescales for making and breaking crosslinks (86) rather than intramolecular reconfiguration times (73). For some systems, kinetically arrested aggregates and rigid solids can form (87–89), whose persistent structure and nonequilibrium properties will require residue-specific interactions and desolvation effects to be accounted for (73, 90–92).

Two important factors contribute to the success of the simple mean-field Rouse framework for predominantly viscous condensates: One is the pronounced separation of timescales between contact lifetimes and overall chain dynamics; the resulting time averaging over vast numbers of contacts makes the concept of friction applicable on the timescale of chain reconfiguration. Another is the absence of pronounced sequence patterns in the proteins and polypeptides included in our analysis; as a result of the corresponding effective spatial averaging (Figure 3I), a homopolymer model provides a

reasonable approximation. A promising approach to account for sequence-specific interactions is to quantitatively relate the energetics and dynamics of molecular simulations to the viscoelasticity of condensates (28). An et al. (29) have reported that increased condensate stability correlates with low mobilities (Supplementary Fig. 2B-D) and high viscosities in coarse-grained simulations and employed active learning to identify the influence of amino acid composition and sequence patterning on the dynamic and thermodynamic properties of biomolecular condensates. It has also been suggested to relate the nature of the contacts formed at the residue level to viscoelastic properties via the eigenvalue spectra of Zimm matrices that account for intra- and intermolecular contacts in the Rouse model, albeit not yet in terms of absolute timescales (73, 93). Using experimentally validated atomistic explicit-solvent simulations, as presented here, may enable the development of related approaches with predictive power for absolute timescales and for aspects such as the frictional contribution of electrostatic interactions (94). The relatively simple quantitative relations between dynamics across length- and timescales demonstrated here show that a close link between molecular mechanisms at the nanoscale and the mesoscopic behavior of biomolecular condensates exists.

#### Data availability

Data that is not available as supplementary information can be requested from the corresponding authors.

#### Code availability

Fretica, a custom add-on package for Mathematica version 12.3 (Wolfram Research) was used for the analysis of single-molecule fluorescence data and is available at <https://github.com/SchulerLab>. The code used to calculate the lifetime of residue-residue contacts is available at <https://doi.org/10.5281/zenodo.7967716>.

#### Acknowledgements

We thank Mark Nüesch for help with data analysis, Andreas Vitalis for help with ABSINTH, and Priya Banerjee, Sam Cohen, Hagen Hofmann, William Jacobs, Dmitrii Makarov, Rohit Pappu, Michael Rubinstein, and Andrea Soranno for insightful discussion. This work was supported by the Swiss National Science Foundation (B.S.), the Novo Nordisk Foundation Challenge program REPIN (#NNF18OC0033926, B.S.), the Intramural Research Program of the National Institute of Diabetes and Digestive and Kidney Diseases at the National Institutes of Health (R.B.B.), the Forschungskredit of the University of Zurich (N.G. and M.T.I.), the Ernst Hadorn Foundation (N.G.), and the European Union's Horizon 2020 research and innovation programme under the Marie Skłodowska-Curie grant agreement ID 898228 (A.C.). We utilized the computational resources of Piz Daint and Eiger at the CSCS Swiss National Supercomputing Centre, and of the National Institutes of Health HPC Biowulf cluster (<http://hpc.nih.gov>). Mass spectrometry was performed at the Functional Genomics Center Zurich. FRAP and bead tracking were performed with support of the Center for Microscopy and Image Analysis, University of Zurich.

#### Author contributions

N.G. and B.S. conceived the project. B.S. and R.B.B. supervised the project. N.G. and S.D.G. performed single-

molecule experiments, FCS, and microrheology. N.G., S.D.G. and A.C. characterized binodal curves. S.D.G. and A.C. performed turbidity experiments. A.C., A.S., and N.G. performed protein purification and/or labeling. D.N. developed single-molecule instrumentation and data analysis tools. N.G. and S.D.G. analyzed the experimental data with input from A.C., A.S., B.S., and D.N.. M.T.I. performed the simulations with the help of R.B.B.. M.T.I., R.B.B., and N.G. analyzed the simulations with the help of B.S. and D.N.. N.G. and B.S. tested the polymer models with the help of D.N.. N.G. and M.T.I. prepared the figures. N.G. and B.S. wrote the manuscript with contributions from all authors.

#### **Competing interests**

The authors declare no competing interests.

#### **Additional information**

##### **Materials & Correspondence**

Correspondence and requests for materials should be addressed to N.G., M.T.I., R.B.B., or B.S.

## Methods

### *Sample preparation and labeling*

We used recombinant human histone H1.0 (H1; New England Biolabs, product code M2501S). Poly L-lysine hydrochloride (referred to as K50, MW = 8200 Da, degree of polymerization 45–55) and poly L-arginine hydrochloride (referred to as R50, MW = 9600 Da, degree of polymerization 45–55) were purchased from Alamanda Polymers (Huntsville, AL, USA; catalog numbers 000-KC050, 000-R050). Protamine was purchased from Sigma-Aldrich (product number P4020). Labeled and non-labeled ProT $\alpha$  were prepared as described previously (95). Labeling was achieved by introducing cysteine residues at positions 56 and 110 for attaching fluorophores (detailed protein sequences in Extended Data Table 1). Prior to labeling, the protein was reduced in phosphate-buffered saline (PBS), pH 7, containing 4 M guanidinium hydrochloride (GdmHCl) and 0.2 mM EDTA, using 10 mM Tris(2-carboxyethyl) phosphine hydrochloride (TCEP) for 60 minutes, followed by multiple (5x) buffer exchange steps to a similar PBS solution without TCEP (pH 7, 4 M GdmCl and 0.2 mM EDTA) using centrifugal filters with a 3-kDa molecular mass cutoff (Sigma-Aldrich). Labeling was achieved with Cy3B maleimide (Cytiva) and CF660R maleimide (Sigma-Aldrich) at a protein: dye ratio of 1:6:6, incubated for an hour at room temperature and overnight at 277 K. Excess dye was reacted using 10 mM dithiothreitol for ten minutes and removed by centrifugal filtration. The labeled protein was subsequently purified by reversed-phase high pressure liquid chromatography using a Reprosil Gold C18 column (Dr. Maisch, Germany), without separating the labeling permutants. The correct mass of labeled protein was confirmed by electrospray ionization mass spectrometry.

### *Turbidity measurements*

To assess the extent of phase separation, the relative turbidity was quantified by the attenuation of light at 350 nm with a NanoDrop 2000 UV-Vis spectrophotometer (Thermo Scientific). The positively charged polypeptides were added to a fixed volume of a ProT $\alpha$  solution to achieve a final concentration of 10  $\mu$ M ProT $\alpha$  and investigate a wide range of stoichiometric ratios. These experiments were carried out in TEK buffer, composed of 10 mM Tris-HCl, 0.1 mM EDTA (pH 7.4), with ionic strength adjusted using KCl. Samples were rapidly mixed via pipetting for approximately 10 seconds before measurements. Each sample was measured four times, and the results were averaged. Both protein stock solutions were diluted in identical buffers before the mixing process.

### *Single-molecule fluorescence spectroscopy*

We performed confocal single-molecule analysis, concentration determination, and fluorescence correlation spectroscopy at 295 K with a MicroTime 200 (PicoQuant), equipped with a UPlanApo 60 $\times$ /1.20-W objective (Olympus), mounted on a piezo stage (P-733.2 and PIFOC from Physik Instrumente GmbH), using a 532-nm continuous-wave laser (LaserBoxx LBX-532-50-COL-PP; Oxixus), and a 635-nm diode laser (LDH-D-C-635M; PicoQuant). Fluorescence photons, which were separated from scattered laser light using a triple-band mirror (zt405/530/630rpc from Chroma), were initially divided into two channels by either a polarizing or a 50/50 beam splitter, and then into four detection channels with dichroic mirrors to separate donor and acceptor emission (T635LPXR from Chroma). Donor emission was further filtered with an ET585/65m band-pass (Chroma), and acceptor emission with an LP647RU long-pass filter (Chroma), before being detected by SPCM-AQRH-14-TR single-photon avalanche diodes (PerkinElmer). SymPhoTime 64 version 2.4 (PicoQuant) was used for data acquisition.

In single-molecule measurements, ProT $\alpha$ , labeled with Cy3B and CF660R, was excited by the 532-nm laser. Experiments were conducted in TEK buffer, including varying concentrations of KCl. Plastic sample chambers ( $\mu$ -Slide, ibidi) were used to mitigate surface adhesion of the positively charged polypeptides. For measurements of dilute-phase samples, the power of the 532-nm laser was set to 100  $\mu$ W (measured at the back aperture of the microscope objective); the confocal volume was positioned 30  $\mu$ m deep into the sample chamber; and concentrations of labeled protein between 50 and 100 pM were used. For single-molecule measurements in the dense phase, the average power at the back aperture was between 3 and 30  $\mu$ W for continuous-wave excitation, depending on the background level; the confocal volume was placed at the center of the spherical droplets, whose radii varied between 4 and 30  $\mu$ m. Unlabeled proteins (12  $\mu$ M ProT $\alpha$  and a concentration of the positively charged polypeptides to ensure charge balance) were mixed with 5 to 10 pM of labeled ProT $\alpha$ . Photon bursts, emerging as proteins traversed the confocal volume, were isolated from background-corrected fluorescence trajectories, binned at 4 ms, with a photon count threshold of 285 per burst. In dilute-phase measurements, bursts were defined as sequences of at least 285 consecutive photons with interphoton times below 40  $\mu$ s.

Ratiometric transfer efficiencies were obtained from  $E = N_A / (N_A + N_D)$ , where  $N_A$  and  $N_D$  are the numbers of donor and acceptor photons, respectively, in each photon burst, corrected for background, channel crosstalk, acceptor direct excitation, differences in quantum yields of the dyes, and detection efficiencies (96, 97). Mean transfer efficiencies,  $\langle E \rangle$ , were determined from fits with Gaussian peak functions to the transfer efficiency histograms. To infer dye-to-dye distance distributions,  $P(r)$ , from  $\langle E \rangle$ , we use the relation (53)



$$\langle E \rangle = \langle \varepsilon \rangle \equiv \int_0^\infty \varepsilon(r)P(r)dr, \text{ Eq. 6}$$

where

$$\varepsilon(r) = R_0^6 / (R_0^6 + r^6). \quad \text{Eq. 7}$$

The Förster radius,  $R_0$ , (98) of 6.0 nm for Cy3B/CF660R in water (99) was corrected for the refractive index,  $n$ , in the droplets according to the published dependence of  $n$  on the protein concentration (100), which is linear up to a mass fraction of at least 50 % (101) and only marginally dependent on the type of protein (100). At the dense-phase protein concentrations,  $n$  is greater than in water by 3%–6%, resulting in a slightly smaller  $R_0$  inside the droplets (5.8–5.9 nm). Systematic uncertainties in transfer efficiencies due to instrument calibration and uncertainty in  $R_0$  are estimated to be roughly  $\pm 0.03$ , in line with the range previously reported (96). The precision for measurements on the same instrument is higher, typically  $< 0.01$  (99).  $P(r)$  was estimated using the length scaling exponent  $\nu$  by applying an empirically modified self-avoiding-walk polymer (SAW- $\nu$ ) model (102, 103). To estimate the mean square end-to-end distance of the complete ProT $\alpha$  chain, we used  $\nu$  and the total number of amino acids,  $N_{tot} = 110$ ]. The impact of fluorophore labeling on ProT $\alpha$ -H1 interaction was minimal, as evidenced by previous studies (57, 95), and given the fraction of  $< 10^{-6}$  of labeled protein in the dense phases, effects of fluorophore labeling on dense-phase behavior were considered negligible. Analysis of fluorescence data was performed with the software package Fretica (<https://github.com/SchulerLab>) run with Mathematica 12.3 (Wolfram Research).

#### *Measurements of protein concentrations and diffusion coefficients in the dilute and dense phases*

We utilized fluorescence correlation spectroscopy (FCS) and quantitative fluorescence intensity analyses using a MicroTime 200 (PicoQuant) to assess the concentrations of ProT $\alpha$  molecules doubly labeled with Cy3B and CF660R, in the dense and dilute phases (36, 74). A mixture of unlabeled proteins (12  $\mu\text{M}$  ProT $\alpha$  and a concentration of the respective positively charged polypeptides to ensure charge balance), doped with a small concentration ( $\sim 10$  pM to 10 nM) of labeled ProT $\alpha$  in TEK buffer including the specified concentrations of KCl was allowed to phase-separate at 295 K. To analyze the dilute phase, the phase-separated mixture was centrifuged at 295 K for 30 minutes at 25,000 g, leading to the formation of a single large droplet from the dense phase. The supernatant was then aspirated and placed into a sample chamber ( $\mu$ -Slide, ibidi). For measurements in the dense phase, the phase-separated mixture was directly transferred to the sample chamber, and droplets were allowed to settle on the bottom surface of the sample chamber by gravity; the boundaries of individual droplets were identified via 3D confocal imaging, and FCS and intensity measurements were performed by focusing inside the droplets.

To excite CF660R, we employed the 635-nm continuous-wave laser at 5  $\mu\text{W}$  (measured at the back aperture of the objective). The emitted fluorescence photons were then separated using a polarizing beam splitter and subsequently detected by two detectors. The collected correlation data were analyzed employing a model that assumes a 3D Gaussian-shaped confocal volume:

$$G(\tau) = G_0 \left[ \left( 1 + \frac{\tau}{\tau_D} \right) \sqrt{1 + s^{-2} \frac{\tau}{\tau_D}} \right]^{-1}, \quad \text{Eq. 8}$$

where  $\tau$  is the lag time,  $G_0$  is the amplitude,  $\tau_D$  is the translational diffusion time, and  $s$  is the ratio of the axial to lateral radii of the confocal volume. The calibration curve was generated from the analysis of samples with known concentrations (0.3, 1, 3, 10, 30, and 100 nM) of labeled ProT $\alpha$  in TEK buffer including 120 mM KCl.

Concentrations were estimated from the average number of labeled proteins in the confocal volume,  $N_p = \left( 1 - \frac{n_b}{n_f} \right)^2 / G_0$ , as previously described (74), where  $n_b$  is the background count rate estimated from samples without labeled protein, and  $n_f$  is the average count rate of the measurement with labeled ProT $\alpha$ . As an alternative method for estimating concentrations, the fluorescence intensity after background subtraction was used based on a corresponding calibration curve. Total ProT $\alpha$  concentrations were obtained by dividing the concentrations of labeled ProT $\alpha$  by the doping ratio, which was set to ensure that fluorescence intensities fell within the range of linear response of detection. This approach requires higher doping ratios for measurements in the dilute phase than for those in the dense phase. For each set of experimental conditions, a minimum of two concentration estimates were made, one using FCS and one using intensity detection. These assessments were repeated a minimum of two times to increase reliability. Diffusion coefficients were calculated from translational diffusion times,  $\tau_D$ , using a calibration curve

$$D = \frac{\Lambda}{\tau_D},$$

Eq. 9

where  $\Lambda$  was obtained from a calibration with samples of known diffusion coefficient in water. The calibration was cross-validated in ProT $\alpha$ -H1 droplets with two-focus FCS (104) to account for effects of refractive index differences between dilute and dense phase on the observed translational diffusion coefficients (36).

Since maximum dense phase formation occurs at a mixing ratio close to charge balance (Supplementary Fig. 1), all experiments were performed by mixing ProT $\alpha$  and the positively charged polypeptides at this ratio. Since reproducible droplet formation becomes difficult to maintain and exceedingly sample consuming at salt concentrations near the critical point, a compromise between experimental feasibility and accessible salt concentrations was made.

### Microrheology

We mixed ProT $\alpha$  and the positively charged polypeptides, both unlabeled, under phase separating conditions at charge balance with an aliquot of fluorescent microspheres (100 nm and 500 nm diameter, Fluoro-Max, Thermo Fisher Scientific). After centrifugation, we collected a single large droplet (diameter  $\geq 100 \mu\text{m}$ ) for observation. Tracking the motion of the beads within the droplet was conducted at 295 K using an Olympus IXplore SpinSR10 microscope equipped with a 100 $\times$ /1.46 NA plan-apochromat oil immersion objective, for 300 seconds with 50 ms exposure time per image and an acquisition rate of 5 Hz. Bead trajectories were obtained using the TrackMate plugin of Image J (105) and further analyzed with MATLAB 2016b (MathWorks). We calculated the mean square displacements (MSD) in the image plane, averaging across 20 trajectories, to obtain the diffusion coefficient,  $D$ , from  $\langle \text{MSD}(t) \rangle = 4Dt$ , where  $t$  is the time after the start of observation.

The MSD analysis demonstrates uniform viscous properties within the droplets, as evidenced by the Brownian diffusion, the consistency between different beads probed in the droplet volume, and the uniform fluorescence intensity observed in microscopy images. We did not observe aging effects on the timescale up to days. We estimated the viscosity,  $\eta$ , using the Stokes–Einstein equation assuming freely diffusing Brownian motion of particles with hydrodynamic radius  $R_h$ :

$$\eta = \frac{k_B T}{6\pi D R_h}.$$

Eq. 10

In this study, we were interested on the bulk viscosity of the medium that can be measured by probes that are much larger than the correlation length of the polymer network (106, 107). At short times, some MSD curves apparently deviate from the linear Brownian behavior. This effect is due to uncertainties in position determination owing to out-of-focus beads (Supplementary Fig. 3C, D), rather than due to possible elastic properties of the dense phase, which cannot be resolved within the time scales studied here (72).

To increase the time resolution of tracking, we also tested K50-ProT $\alpha$  droplets in an optical tweezers instrument (C-Trap, LUMICKS, Amsterdam). K50-ProT $\alpha$  was the sample least prone to photodamage by the IR laser. A condensate-forming sample (3  $\mu\text{l}$ ) mixed with 1- $\mu\text{m}$  polystyrene beads was placed on a polymer coverslip (ibidi GmbH, Germany) at the center of an enclosure formed by double-sided tape. Another polymer coverslip was placed on top of the sample, sandwiching and sealing it. The condensate sample was left to equilibrate for 30 min. The sample was then placed on the sample stage of the optical tweezers instrument equipped with a 60 $\times$  water immersion objective and a bright-field camera. We trapped isolated beads within large droplets (diameter  $> 50 \mu\text{m}$ ) with minimal laser power to prevent photodamage and the formation of optically visible bubbles at the bead surface. Beads motion was recorded with the camera at  $> 300 \text{ Hz}$  and tracked with Blulake (LUMICKS, Amsterdam). MSDs were calculated in Mathematica (Wolfram Research).

### Correlation length, overlap concentration, and entanglement concentration

The correlation length in the dense phase was estimated from  $\xi \approx R_g (c_p/c^*)^{-\nu/(3\nu-1)}$  (22), where  $c_p$  represents the total protein concentration (concentration of ProT $\alpha$  plus the concentration of the positively charged partner);  $c^*$  is the overlap concentration, defined as  $c^* = 1/V$  with  $V$  approximating the volume occupied by a polymer chain ( $V \approx 4/3 \pi R_g^3$ );  $R_g$  is the radius of gyration ( $R_g \approx \sqrt{\langle R^2 \rangle} / \sqrt{6}$ , where  $\sqrt{\langle R^2 \rangle}$  is the mean square end-to-end distance of the polymer); and  $\nu$  is the scaling exponent. The condition  $c_p \geq c^*$  delineates the dilute from the semidilute regime, marking the beginning of chain interpenetration (22, 108). The concentrations corresponding to  $c^*$  in our samples range from 7 mM to 10 mM, while the protein concentrations corresponding to  $c_p$  in the four samples range from 14 mM to 42 mM (concentration averages at the different protein compositions and salt concentrations). The correlation lengths are between 1 nm and 5 nm; this range was estimated using the average values of  $R_g$  and  $c_p$  for the four protein combinations at the different salt concentrations; values of  $\nu$  ranging from 0.5 to 0.6; and values of  $c^*$  based on the lower and upper bounds of both  $R_g$  and the theoretical limits for the hydrodynamic radius ( $R_g / 1.5 < R_h < R_g / 0.77$ ) (22, 109) as chain dimensions.

Obtaining a precise measured value of  $\nu$  is challenging; from internal length scaling of the disordered proteins in the MD simulations (109), we estimate values of  $\nu$  ranging from 0.53 to 0.63 for the different coacervates and salt concentrations. Since  $c_p > c^*$  for all conditions used, the correlation lengths are thus smaller than the chain dimensions, we expect excluded volume interactions to be screened by the overlapping chains on the length scales we are probing experimentally (22). Similarly, hydrodynamic interactions are expected to be screened under these conditions, indicating that Rouse dynamics apply on the length scales of entire chains (22, 108). For consistency and simplicity, we thus use the corresponding value of  $\nu = 1/2$  throughout. The entanglement concentration,  $c_e$ , delineates the transition from a non-entangled polymer solution to an entangled one when  $c_p \gtrsim c_e$ . This condition is met approximately if the protein concentration is high enough that there are at least two chains in the volume  $V$  pervaded by a single chain (see eq. 10 in ref. (68)), yielding  $c_e \approx 2c^*$ . As  $c_p \approx c_e$  in our systems, only mild entanglement effects are expected. Total volume fractions of protein,  $\phi$ , were calculated from the measured ProT $\alpha$  concentrations,  $c_{\text{ProT}\alpha}$  (Figure 1E), as  $\phi = (M_{w,\text{ProT}\alpha} c_{\text{ProT}\alpha} \bar{v}_{\text{ProT}\alpha} + X M_{w,\text{partner}} c_{\text{ProT}\alpha} \bar{v}_{\text{partner}})$ , where  $M_w$  is the molecular weight,  $\bar{v}$  is the partial specific volume, and  $X$  is the mixing ratio between the positively charged partner and ProT $\alpha$  to reach charge balance. We note that since the samples examined here are complex coacervates of similar but not identical lengths, the values must be considered approximate.

### Nanosecond fluorescence correlation spectroscopy (nsFCS)

Samples for nsFCS measurements were prepared as outlined in the section *Single-molecule measurements*. To avoid the reduction in signal due to photobleaching of slowly diffusing molecules in the dense phase, we moved the confocal volume at constant speed (3  $\mu\text{m/s}$ ) following a serpentine trajectory in a horizontal plane within the droplet (36). Excitation with continuous-wave laser light of 532 nm was conducted at 3 or 30  $\mu\text{W}$  (measured at the back aperture of the objective). For subpopulation-specific correlation analysis of the FRET-active species, we used photons from bursts with  $\langle E \rangle > 0.15$ . Autocorrelation curves of acceptor ( $A$ ) and donor ( $D$ ) detection channels, and cross-correlation between  $A$  and  $D$  were analyzed as described previously (36, 110). In Figure 2E we show cross correlation curves with logarithmically spaced lag times ranging from nanoseconds to milliseconds. The function used for fitting the correlations between detection channels  $i, j = A, D$  is

$$G_{ij}(\tau) = G_{0,ij} \frac{(1 - c_{ab}^{ij} e^{-|\tau|/\tau_{ab}^{ij}})(1 + c_{cd}^{ij} e^{-|\tau|/\tau_{cd}})(1 + c_{rot}^{ij} e^{-|\tau|/\tau_{rot}})}{\left(1 + \frac{|\tau|}{\tau_D}\right) \left(1 + s - 2\frac{|\tau|}{\tau_D}\right)^{1/2}}. \quad \text{Eq. 11}$$

The three terms in the numerator with amplitudes  $c_{ab}^{ij}$ ,  $c_{cd}^{ij}$ ,  $c_{rot}^{ij}$ , and correlation times  $\tau_{ab}^{ij}$ ,  $\tau_{cd}$ ,  $\tau_{rot}$  describe photon antibunching, conformational dynamics, and dye rotation, respectively.  $\tau_D$  and  $s$  are defined as in Eq. 8. Conformational dynamics result in a characteristic pattern with a positive amplitude in the autocorrelations ( $c_{cd}^{DD} > 0$  and  $c_{cd}^{AA} > 0$ ) and a negative amplitude in the cross-correlation ( $c_{cd}^{AD} < 0$ ), but with a common correlation time  $\tau_{cd}$ . The three correlation curves  $G_{DD}(\tau)$ ,  $G_{AA}(\tau)$ , and  $G_{AD}(\tau)$  were fitted globally with  $\tau_{cd}$  and  $\tau_{rot}$  as shared fit parameters. The relaxation time  $\tau_{cd}$  was converted into the chain reconfiguration time  $\tau_r = \int_0^\infty \frac{\langle r(0)r(\tau) \rangle}{\langle r^2 \rangle} d\tau$ , according to the procedure previously established (111). This conversion is based on the assumption that dynamics of the inter-dye distance  $r$  can be represented as diffusive motion in a potential of mean force obtained from the distance distribution  $P(r)$  by Boltzmann inversion (52, 111).

The experimental uncertainties of  $\tau_r$  reported here are either standard deviations calculated from three measurements or the error of the fit of  $\tau_{cd}$  (from which  $\tau_r$  is derived), whichever was greater. We estimate the error of the fit from the variability resulting from fits using different lag-time intervals of the FCS data: We report as uncertainties the range of reconfiguration times obtained by using values from 0.8 ns to 8 ns as lower bounds, and from 1 ms to 6 ms as a upper bounds of the fitting window. The rotational correlation time,  $\tau_{rot}$ , is approximately one order of magnitude smaller than the chain reconfiguration time,  $\tau_r$ , and is caused by dye rotation (36).

### Polymer models

We compared the experimental results of ProT $\alpha$  reconfiguration times  $\tau_r$  and ProT $\alpha$  translational diffusion coefficients  $D$  in condensates, together with the emerging bulk viscosities  $\eta$  of the condensates, with corresponding values derived from three models commonly used for polymer solutions, dilute solutions, and polymers in a network of obstacles: i) the Rouse model (21), ii) the Zimm model (112), and iii) the Rouse model with entanglement (66, 69, 70). Since the concentrations and chain dimensions in the dense phases are comparable in all systems studied, we tested the models using average values of these quantities rather than reduced quantities, which would not have allowed a comparison of different models with different dependencies on protein concentrations and chain dimensions for all samples



together. The upper and lower limits of the error bands in Figure 4D correspond to models calculated for the minimum and maximum values of the chain dimensions and protein concentrations in the set of experimentally observed values.

i) The Rouse model describes the dynamics of a chain of  $N$  beads connected by harmonic springs with root mean square length  $b$ , and subjected to Brownian motion with friction coefficient  $\zeta$ . The friction of the whole chain is approximated as  $N\zeta$ . The translational diffusion coefficient of the center of mass of the entire chain  $D$  is given by the Einstein relation,

$$D = \frac{k_B T}{N\zeta}. \quad \text{Eq. 12}$$

The longest relaxation time of the Rouse chain is (see ref. (66), eq. 4.37)

$$\tau_R = \frac{\zeta N^2 b^2}{3\pi^2 k_B T} = \frac{\langle R^2 \rangle}{3\pi^2 D}. \quad \text{Eq. 13}$$

For the second term, we used  $\langle R^2 \rangle = Nb^2$  and Eq. 12.  $\tau_R$  is related to the vector reconfiguration time  $\tau_{ij}$  of the experimentally probed segment between residues  $i = 56$  and  $j = 110$  of ProT $\alpha$ . This time is defined as a vector correlation time  $\tau_{ij} = \int_0^\infty \langle \mathbf{r}_{ij}(0) \cdot \mathbf{r}_{ij}(t) \rangle / \langle r_{ij}^2 \rangle dt$ , where  $\mathbf{r}_{ij}$  is the vector between the positions of the two residues. Makarov found the useful relation (113)

$$\tau_{ij} / \tau_R = \frac{\pi^2}{24} |\mu - \lambda| \{ -(4 + 7\mu^2 - 12\lambda + 7\lambda^2 - 12\mu + 10\mu\lambda) + 4 - 4|\mu - \lambda| + (\mu - \lambda)^2 \}, \quad \text{Eq. 14}$$

where, in our case,  $\mu = \frac{i}{N_{\text{ProT}\alpha}}$  and  $\lambda = \frac{j}{N_{\text{ProT}\alpha}}$ ; with  $N_{\text{ProT}\alpha} = 112$ , we obtain  $\frac{\tau_{ij}}{\tau_R} = 0.54$ . Note that  $\tau_{ij}$  is not identical to the reconfiguration time,  $\tau_r$ , because the latter is defined as a distance correlation time  $\tau_r = \int_0^\infty \langle r_{ij}(0) \cdot r_{ij}(t) \rangle / \langle r_{ij}^2 \rangle dt$ , where  $r_{ij}(t) = |\mathbf{r}_{ij}(t)|$  is the length of the vector. We are not aware of an analytical relation between  $\tau_r$  and  $\tau_{ij}$ . To assess the relation between the two times, we simulated the dynamics of Rouse chains, each for five million time steps, with different numbers of segments,  $N$ , ranging from 10 to 40, and with different ratios between the size of the time steps and the friction coefficients (ranging from 0.4 to 4) and found that the distance decorrelation time is smaller than the vector decorrelation time by a factor  $\Xi = \frac{\tau_r}{\tau_{ij}} = 0.50 \pm 0.05$  (error is s.d. from 24 different simulations). It follows that the expected relation between the measured reconfiguration time,  $\tau_r$ , and the Rouse time,  $\tau_R$ , is in our case:

$$\tau_r \approx \Xi \cdot 0.54 \cdot \tau_R = 0.27 \cdot \tau_R. \quad \text{Eq. 15}$$

The bulk viscosity of a polymer solution (21, 66) is given by (see eq. 32 in ref. (21) and eq. 7.33 in ref. (66)):

$$\eta = \frac{c\zeta}{36} Nb^2 + \eta_s = \frac{k_B T c_p \langle R^2 \rangle}{36 D} + \eta_s \quad \text{Eq. 16}$$

where  $c_p = c/N$  is the concentration of protein molecules in the condensates (number of protein molecules per volume),  $c$  is the concentration of chain segments (number of segments per volume) in the condensates, and  $\eta_s$  is the bulk solvent viscosity (1 mPa s in our samples). The relation between reconfiguration time and viscosity is given by combining Eq. 13, Eq. 15, and Eq. 16. The error bands in Figure 4D represent the results of the models calculated from the range of experimental chain dimensions, protein concentrations, and  $\Xi$ .

ii) The Zimm model extends the Rouse model by including hydrodynamic interactions. It recognizes that the motion of one part of the polymer chain affects the surrounding solvent, which in turn affects the motion of other parts of the chain; the Zimm model is thus considered appropriate for polymers in dilute solution. Based on the arguments presented above, we expect our coacervates to be in the Rouse regime, but since correlation lengths and chain dimensions are in a similar range, we present the analysis based on the Zimm model for direct comparison. The Zimm model relates the diffusion coefficient,  $D$ , and the chain reconfiguration time,  $\tau_Z$ , to the solvent viscosity (see eq. 4.61 and 4.63 in ref. (66)), but if the viscosity in the polymer network is length scale-dependent (36), the relations can be inverted to obtain an effective solvent viscosity,  $\eta_Z$ , at the length scale of the chain relevant for polymer dynamics:

$$\eta_Z = \frac{8}{3\sqrt{6}\pi^3} \frac{k_B T}{\sqrt{\langle R^2 \rangle} D}, \quad \text{Eq. 17}$$

which is equivalent to the Stokes-Einstein equation (Eq. 10) with  $R_h = \frac{3\sqrt{\pi}}{8\sqrt{6}} \sqrt{\langle R^2 \rangle} \approx \frac{2}{3} R_g$ ,

$$\eta_Z = \frac{\sqrt{3\pi} k_B T \tau_1}{\sqrt{\langle R^2 \rangle^3}} \quad \text{Eq. 18}$$

$$\text{and } \tau_Z = \frac{8}{9\pi^2 \sqrt{2}} \frac{\langle R^2 \rangle}{D}. \quad \text{Eq. 19}$$

However, in contrast to the Rouse model with entanglement (see iii), Zimm theory can only describe part of the relations we observe experimentally (Supplementary Fig. 7B).

iii) The Rouse model with entanglement (66, 69, 70) considers a Rouse chain diffusing in a network of other chains resulting in obstacles effectively forming tubes of diameter  $a$ , within which the chain can diffuse, where  $a$  can be considered the 'entanglement spacing' (71) (Figure 4C). In this picture, the center-of-mass diffusion coefficient of the chains,  $D$ , depends both on the friction coefficient,  $\zeta$ , acting on individual beads, and on the ratio between the entanglement spacing and the chain dimensions (see eq. 6.40 in ref. (66)),

$$D = \frac{k_B T a^2}{3N\zeta \langle R^2 \rangle}. \quad \text{Eq. 20}$$

The viscosity of the polymer solution can thus be expressed in terms of  $D$  (see eq. 7.47, 7.43, 6.19 and 6.40 in ref. (66)) as

$$\eta = \frac{k_B T c_p \langle R^2 \rangle \langle R^2 \rangle}{36 D a^2} + \eta_s, \quad \text{Eq. 21}$$

and can be used to calculate the entanglement spacing for all samples (Supplementary Fig. 7A), resulting in  $a = 4 \pm 1$  nm ( $\pm 1$  nm is the variability among the samples), which is of the same order as the correlation length,  $\xi$ , estimated for the dense phases. The error bands in Figure 4D account for the slightly different entanglement spacing, chain dimensions, and concentrations in the different samples.

There are three characteristic times for chain relaxation (compare to eq. 6.106, 6.18, 6.19 in ref. (66)):  $\tau_e = \frac{a^6}{3\langle R^2 \rangle^2 D}$  is the time at which the displacement of chain segments becomes comparable to the entanglement spacing,  $a$ ;  $\tau_{\text{Rtube}} = \frac{a^2}{9\pi^2 D}$  is the time for chain relaxation within a tube;  $\tau_d = \frac{\langle R^2 \rangle}{3\pi^2 D}$  is the disentanglement time — the time required for a chain to disentangle from the tube within it was confined. In Supplementary Fig. 7B, we compared the experimental chain reconfiguration time and diffusion coefficient with the three characteristic times of an entangled chain with tube diameter of  $a = 4$  nm and found that the chain relaxation that best describes the experimental results is  $\tau_d$ . This means that the major contribution to end-to-end distance fluctuations is due to protein disentanglement. Note that  $\tau_d$  and  $\tau_R$  defined for the Rouse model have the same dependence on  $D$ .

The viscosity of the polymer solution can also be obtained from the chain relaxation times by combining Eq. 21 with the three relations for  $\tau_e$ ,  $\tau_{\text{Rtube}}$ , and  $\tau_d$ . The finding that  $\tau_r \approx \tau_d$  is valid both for the relation between chain reconfiguration time and diffusion coefficient (Eq. 4), and for the relation between chain reconfiguration time and viscosity (Eq. 5, Supplementary Fig. 7B). For consistency with section i), in Figure 4D and Supplementary Fig. 7B, we scaled  $\tau_e$ ,  $\tau_{\text{Rtube}}$ , and  $\tau_d$  relative to  $\tau_r$  as described for  $\tau_R$  in Eq. 15.

### *Molecular dynamics (MD) simulations*

All-atom explicit solvent simulations of phase-separated ProT $\alpha$ -H1 in 8 mM KCl as well as ProT $\alpha$ -protamine in 8 mM KCl and 128 mM KCl were performed using the same simulation parameters as previously described for phase-separated ProT $\alpha$ -H1 at 128 mM KCl (36). In brief, we employed the Amber99SBws force field (114, 115) with the TIP4P/2005s water model (116, 117). The temperature was kept constant at 295.15 K using stochastic velocity rescaling (118) ( $\tau = 1$  ps), and the pressure was kept at 1 bar with a Parrinello-Rahman barostat (119). Long-range electrostatic interactions were modeled using the particle-mesh Ewald method (120) with a grid spacing of 0.12 nm and a real-space cut-off of 0.9 nm. Dispersion interactions and short-range repulsion were described by a Lennard-Jones potential with a cutoff at 0.9 nm. Bonds involving hydrogen atoms were constrained to their equilibrium lengths using the LINCS algorithm (121). Equations of motion were integrated with the leap-frog algorithm with a time step of 2 fs, with initial velocities taken from a Maxwell-Boltzmann distribution at 295.15 K. All simulations were performed using GROMACS (122) version 2021.5. We simulated the unlabeled variant of ProT $\alpha$ , since the droplets under experimental conditions had 1000-fold higher concentration of unlabeled than labeled ProT $\alpha$ .

To obtain the starting structure of phase-separated ProT $\alpha$ -H1 at the desired ion concentration of 8 mM KCl, and to ensure charge neutrality, we removed 2289 potassium and 2289 chloride ions from the snapshot at 5  $\mu$ s of our

previous phase-separated ProTα-H1 at 128 mM KCl (36). The simulation system contained 96 ProTα and 80 H1 molecules, 129 potassium and 241 chloride ions, and 899,220 water molecules, resulting in a simulation system of 3,996,354 particles. The free production run was 3.1 μs long, with a timestep of 2 fs, employing 36 nodes (each consisting of an Intel Xeon E5-2690 v3 processor with 12 cores and an NVIDIA Tesla P100 GPU at the Swiss National Supercomputing Centre) with a performance of ~35 ns/day, corresponding to ~3 months of supercomputer time. The first 2.1 μs were treated as system equilibration and not used for the analysis.

For the ProTα-protamine simulations, the initial structure for all-atom simulations of the phase-separated system in slab configuration (55) was obtained with coarse-grained (CG) simulations, following the strategy described previously (36). We utilized the one-bead-per-residue model that was previously developed to study the 1:1 ProTα-H1 dimer (57). Briefly, the potential energy has the following form:

$$\begin{aligned}
 V = & \frac{1}{2} \sum_{i < N} k_b (d_{ij} - d_{ij}^0)^2 + \frac{1}{2} \sum_{i < N-1} k_\theta (\theta_{ijk} - \theta_{ijk}^0)^2 \\
 & + \sum_{i < N-2} \sum_{n=1}^4 k_{i,n} (1 + \cos(n\phi_{ijkl} - \delta_{i,n})) + \sum_{a < b} \frac{q_a q_b}{4\pi\epsilon_a \epsilon_0 d_{ab}} \exp\left[-\frac{d_{ab}}{\lambda_D}\right] \\
 & + \sum_{(a,b)} 4\epsilon_{pp} \left( \left(\frac{\sigma_{ab}}{d_{ab}}\right)^{12} - \left(\frac{\sigma_{ab}}{d_{ab}}\right)^6 \right),
 \end{aligned} \tag{Eq. 22}$$

where  $i, j, k, l$  denote consecutive residues. The first term represents the harmonic bond energy with force constant  $k_b = 3.16 \times 10^5 \text{ kJ mol}^{-1} \text{ nm}^{-2}$ , and the second term represents the angle energy with force constant  $k_\theta = 6.33 \times 10^2 \text{ kJ mol}^{-1} \text{ rad}^{-2}$ ; reference values for  $d_{ij}^0$  and  $\theta_{ijk}^0$  were taken from an extended backbone structure (0.38 nm;  $2\pi/3$  rad). The third term represents a sequence-based statistical torsion potential taken from the Go model of Karanicolas and Brooks (123), which was applied to all residues. The fourth term represents a screened coulomb potential, with Debye screening length  $\lambda_D$ , applied to all residues with non-zero charges  $q_i$ ;  $\epsilon_0$  is the permittivity of free space; the dielectric constant,  $\epsilon_a$ , was set to 80. The fifth term represents a generic short-range attractive potential applied to all residue pairs. This interaction is characterized by a contact distance  $\sigma_{ab} = (\sigma_a + \sigma_b)/2$ , where  $\sigma_{a,b}$  are the residue diameters (all ~0.6 nm) determined from residue volumes (124), and a contact energy  $\epsilon_{pp}$ , which is the same for all residue pairs and was set to  $0.16 k_B T$ , or  $\sim 0.40 \text{ kJ/mol}^{-1}$ . The Debye length,  $\lambda_D$ , is given by

$$\lambda_D = \left( \frac{\epsilon_a \epsilon_0 k_B T}{2e^2 I} \right)^{1/2}, \tag{Eq. 23}$$

where  $k_B$  is the Boltzmann constant,  $T$  the temperature,  $e$  the elementary charge, and  $I$  the ionic strength.

Using this coarse-grained model, 96 ProTα and 197 protamine molecules (1:1 charge balance) in an initially extended configuration were placed on a rectangular grid in a 60-nm cubic box, and the energy of the system was minimized with the steepest-descent algorithm. The system was further relaxed in a short NVT run at 500 K and an implicit ionic strength of 500 mM. In the next step, the box edge was decreased to 22.41 nm in a 56-ps NPT run with reference pressure set to 20 bar to obtain an average protein density close to that of the dense phase in experiment. The system configuration was further randomized via a 1.5-μs NVT run (using a 10-fs time step) at 500 K and an implicit ionic strength of 500 mM to ensure relatively uniform protein density in the box. Each chain from the final CG structure was independently reconstructed in all-atom form using a lookup table from fragments drawn from the PDB, as implemented in Pulchra (124). Side-chain clashes in the all-atom representation were eliminated via a short Monte Carlo simulation with CAMPARI (125) using the ABSINTH energy function (125), in which only the side chains were allowed to move. Due to the large number of proteins and the relatively high density of proteins in the box, the first CAMPARI moves were performed using a soft-core Lennard-Jones (LJ) potential, which has an energy cap, thus avoiding the very large energies resulting from the exclusion in the first Monte Carlo moves at the beginning of the CAMPARI simulation. Subsequently, the soft-core LJ potential was gradually transformed into a global soft-core form by increasing the CAMPARI parameters FMCSF\_FEG\_IPP and FMCSF\_FEG\_ATTJ. The following pairs of FMCSF\_FEG\_IPP and FMCSF\_FEG\_ATTJ values were used: 0.5 and 0.35, 0.7 and 0.6, 0.9 and 0.85, 0.95 and 0.92, 0.98 and 0.96, 0.99 and 0.97, 0.9925 and 0.975, 0.995 and 0.99. Taking the relaxed configuration obtained with CAMPARI, the box edge was extended to 41 nm in the Z direction, and the resulting system was set up with the all-atom Amber ff99sbws protein force field (114, 115) in GROMACS and energy-minimized using the steepest-descent algorithm. To eliminate any non-proline cis-bonds that might have emerged during all-atom reconstruction, we ran a short simulation in vacuum with the dielectric constant set to 80 with periodic boundaries, using a version of the force



field that strongly favors trans peptide bonds (55) and applying weak position restraints to the protein backbone atoms and dihedral angles (5 kJ/mol/rad).

Subsequently, the simulation box was filled with TIP4P/2005s water<sup>44</sup> and energy-minimized. Up to this point, the same setup was used for both 8 mM and 128 mM ProTα-protamine simulations. In the next step, 1587 potassium and 1596 chloride ions were added to the simulation box for ProTα-protamine at 128 mM KCl (2,612,851 particles in total), and 99 potassium and 108 chloride ions were added to the simulation box for ProTα-protamine at 8 mM KCl (2,621,779 particles in total), to match the ionic strength of the buffer used in the experiments and to ensure charge neutrality. In the next step, both systems were again energy-minimized, and a 10-ns MD run was performed with strong position restraints on protein backbone atoms ( $10^5$  kJ mol<sup>-1</sup> nm<sup>-2</sup>) to stabilize the trans isomer for any peptide bonds that had isomerized in the previous step. The final structures of these 10-ns runs with backbone restraints were used for the production runs (without restraints), using GROMACS (122) version 2021.5. The free production runs at 128 mM and 8 mM KCl were ~2.5 μs long, with a timestep of 2 fs, employing 48 nodes each (each node consisting of an Intel Xeon E5-2690 v3 processor with 12 cores and an NVIDIA Tesla P100 GPU at the Swiss National Supercomputing Centre) with a performance of ~63 ns/day, corresponding to ~40 days of supercomputer time. The first 1.5 μs of both simulations were treated as system equilibration and not used for the analysis.

### Analysis of MD simulations

To estimate long-timescale dynamics and correlation functions from the condensate trajectories, the dynamics of each Prothymosin-α chain was described as one-dimensional diffusion along the coordinate defined by the separation in space,  $r$ , of the residues that were dye-labeled in experiment (here we use the distance between Cα atoms of residues 58 and 112). That is, this coordinate is considered to diffuse on a free energy surface,  $F(r)$ , with a diffusion coefficient  $D$  (more generally, position-dependent  $D(r)$ ), whose parameters we determine from the simulations. This distance coordinate is first discretized into  $b$  bins of equal width, from which the number of transitions,  $N_{ji}(\Delta t)$ , from bin  $i$  to bin  $j$  after a lag  $\Delta t$  during the simulations is counted. These statistics are combined from all Prothymosin-α chains, considering that they are expected to be indistinguishable. Discretized free energies and diffusion coefficients were optimized via Monte Carlo simulation using the likelihood function

$$\ln L = \sum_{i,j} N_{ji}(\Delta t) \ln p(j, t + \Delta t | i, t), \quad \text{Eq. 24}$$

where the propagators  $p(j, t + \Delta t | i, t)$  describing the conditional probability of being in bin  $j$  at time  $\Delta t$  after having been in bin  $i$  are obtained from the discretized diffusion model as previously described (126, 127): in short, the discretized dynamics is mapped to a chemical kinetics scheme describing evolution of populations in the bins,  $\dot{\mathbf{P}}(t) = \mathbf{K}\mathbf{P}(t)$ , where  $\mathbf{P}(t)$  is the vector of the bin populations at time  $t$  and  $\mathbf{K}$  is a rate matrix derived from the diffusion coefficient(s)  $D$  (or  $D_i$  for position-dependent  $D$ ) and free energies  $F_i$  associated with each bin according to the scheme of Bicout and Szabo (126, 128). The propagators are then given by  $p(j, t + \Delta t | i, t) = (\exp[\Delta t \mathbf{K}])_{ji}$ . In estimating the most probable parameters from the data, a uniform prior is used for the diffusivities and free energies. The statistical error on the derived parameters is determined by generating synthetic data sets with the same number  $M$  of individual distance trajectories  $r(t)$  as the original, specifically by choosing  $M$  trajectories randomly with replacement, and refitting the model. The error is taken as the standard deviation of the parameters across all synthetic data sets (129).

We can compute the normalized correlation functions directly from the discretized diffusion model via (130)

$$C(t) = \frac{\sum_{n=2}^b (\mathbf{r} \cdot \boldsymbol{\Psi}_n^R)^2 \exp[\lambda_n t]}{\sum_{n=2}^b (\mathbf{r} \cdot \boldsymbol{\Psi}_n^R)^2}, \quad \text{Eq. 25}$$

where the elements of  $\mathbf{r}$  are the centers of each bin on the distance coordinate,  $\boldsymbol{\Psi}_n^R$  is the  $n$ th right eigenvector of  $\mathbf{K}$  ( $\boldsymbol{\Psi}_1^R$  is the stationary eigenvector), and  $\lambda_n$  is the  $n$ th eigenvalue. Similarly, the correlation times are given by

$$\tau_c = - \frac{\sum_{n=2}^b (\mathbf{r} \cdot \boldsymbol{\Psi}_n^R)^2 \lambda_n^{-1}}{\sum_{n=2}^b (\mathbf{r} \cdot \boldsymbol{\Psi}_n^R)^2}. \quad \text{Eq. 26}$$

Errors in correlation functions and correlation times were estimated using the same procedure as for the diffusion model parameters. In our application of the method to the condensate trajectories, we have used 30 equal-width bins between 2 and 10 nm, and a lag time of 200 ns.

A key assumption of this method is that the dynamics is, indeed, well approximated as diffusive after the chosen lag time  $\Delta t$ . If this is true, then the model should become independent of lag time beyond this point. To assess this effect, we computed the correlation time as a function of the lag time and observed that after lag times of around 200 ns it appears to be converging toward a limiting value (Supplementary Fig. 9D). One challenge for using even longer lag times is the limited length of the simulations, resulting in insufficient statistically independent observations.

Separately from the statistical error estimate described above, we also estimated the systematic error associated with the choice of lag time by using correlation times computed at 100 and 300 ns lag times as lower and upper error bars, respectively. A second assumption we have made is that the diffusion coefficient should be uniform, i.e. not dependent on the position on the distance coordinate. This was motivated by our finding that using an explicitly position-dependent diffusion coefficient resulted in very little position dependence, as demonstrated in Supplementary Fig. 9B. Although this conclusion differs from some earlier work (131), this is most likely because we do not significantly sample the very short distances where the position dependence of  $D$  emerged in that study.

The average number of H1/protamine molecules that simultaneously interact with a single ProT $\alpha$  chain, as well as the average number of ProT $\alpha$  chains that simultaneously interact with a single H1/protamine molecule (Fig. 3d) in the dense-phase simulation were quantified by calculating the minimum distance between each ProT $\alpha$  and each H1/protamine for each simulation snapshot. The two molecules were considered to be in contact if the minimum distance between any two of their C $\alpha$  atoms was within 1 nm. Distances between C $\alpha$  atoms were used instead of the commonly used distances between all atoms of the residues to facilitate the large calculations. The 1-nm cutoff between the C $\alpha$  atoms of two residues yields similar results as the commonly used 0.6-nm cutoff for interactions between any pair atoms from the two residues (122). The same contact definition was employed when calculating residue-residue contacts (Fig. 3e): Two residues were considered to be in contact if the distance between their C $\alpha$  atoms was within 1 nm.

Lifetimes of residue-residue contacts were calculated by a transition-based or core-state approach (36, 132). For each pair of residues, a contact was based on the shortest distance between any pair of heavy atoms, one from each residue. Starting from an unformed contact, contact formation was defined to occur when this distance dropped below 0.38 nm; an existing contact was considered to remain formed until the distance increased to more than 0.8 nm (132). Average lifetimes of each residue-residue contact were calculated by dividing the total bound time by the total number of contact breaking events for that contact. Intra-chain contacts were not included in the analysis. Average lifetimes of each pair of ProT $\alpha$ -H1 and ProT $\alpha$ -protamine residues (averaged over the different combinations of ProT $\alpha$  and H1/protamine chains that the two residues could be part of) were calculated by dividing the total contact time (summed over all combinations of ProT $\alpha$  and H1/protamine chains) of a specific residue pair by the total number of the contact breaking events for the same residues (summed over the same combinations of chains). Similarly, to calculate average lifetimes of residue-residue contacts according to the residue type, we first identified all contacts involving a particular pair of residue types, in which one residue was from the ProT $\alpha$  chain and the second was from either H1/protamine or ProT $\alpha$ . Subsequently, the average lifetime of that residue-residue combination was calculated by dividing the total bound time by the total number of contact breaking events for the contacts involving those residue types. Excess populations of contacts between specific types of residues were determined by dividing the average number of observed contacts for a pair of residue types by the value that would be expected if residues paired randomly in a mean-field approximation. The average number of contacts for a pair of residue types was calculated as a sum of all times that residues of those types were in contact, divided by the simulation length. The expected average number of contacts between two residue types (type 1 and 2) was calculated as  $N f(1) f(2)$ , where  $N$  is the average total number of contacts, and  $f(1)$  and  $f(2)$  are the fraction of residues of type 1 and 2, respectively.

The mean squared displacement (MSD) of individual residues within ProT $\alpha$  molecules were calculated as a function of delay time using the Gromacs function *gmx msd*. MSD curves of each ProT $\alpha$  residue for each of the 96 chains in simulations with protamines as well as in simulation with H1 at 8 mM KCl were calculated from the last microsecond of each of the simulations, using residue coordinates every 100 ps. MSD curves of each ProT $\alpha$  residue for each of the 96 chains in ProT $\alpha$ -H1 simulation at 128 mM KCl were calculated previously in four 1- $\mu$ s blocks, using residue coordinates every 100 ps.

All of these analyses are consistent with the previous reports in Galvanetto et al. (36).

Distance distributions of the 1<sup>st</sup>- and the 2<sup>nd</sup>-closest residues (Figure 3H) were computed between all residues of all chains in the simulations. The distances were considered between specific atoms in the side chains: C $\delta$  for glutamate; C $\gamma$  for aspartate; N $\zeta$  for lysine; C $\zeta$  for arginine; and C $\beta$  for alanine. The distributions shown in Figure 3H are averages of 100 structures taken every 1 ns. Percentages of contacts exchanged were calculated by annotating the identity of the 1<sup>st</sup>- and the 2<sup>nd</sup>-closest negatively charged residues (glutamates and aspartates) to all lysine residues in H1-ProT $\alpha$  slab at 128 mM KCl, at time  $t_0$ . Only cases where both the 1<sup>st</sup>- and 2<sup>nd</sup>-closest negatively charged residues ( $X_{1st, t=0}$  and  $X_{2nd, t=0}$ ) were *in contact* with lysines are considered (similar to the contact definition in Figure 3F, distances between reference atoms in the side chains <0.8 nm). We then tracked the distance between the lysines and the two negatively charged residues  $X_{1st, t=0}$  and  $X_{2nd, t=0}$  for 100 ns using residue coordinates every 1 ns, and we annotated whether  $X_{2nd, t=0}$  becomes the 1<sup>st</sup>-closest negatively charged residues to that lysine. The percentage of contacts exchanged in Figure 3K reports the percentage of lysine residues in the system that had two contacts with negatively charged residues at  $t = t_0$  and where  $X_{2nd, t=0}$  became the 1<sup>st</sup> closest negatively charged residue at least once in the

following 100 ns. Error bars are standard deviations of 10 analyses starting at different  $t_0$ . The same analysis was performed for arginine (instead of lysine) in the protamine–ProTα condensate at 128 mM KCl.



## Supplementary figures for

### Mesoscale properties of biomolecular condensates emerging from protein chain dynamics

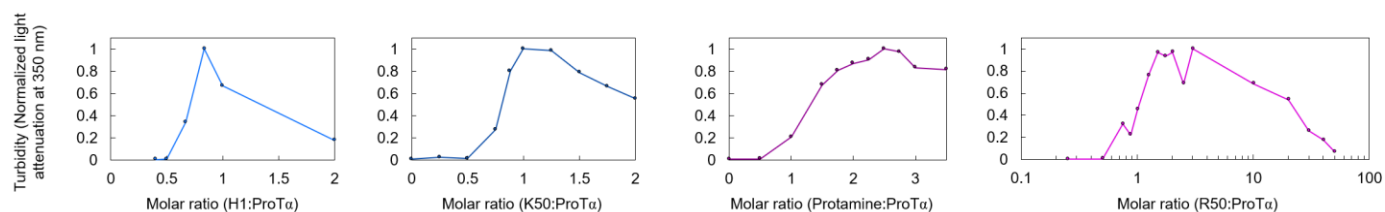
Nicola Galvanetto<sup>1,2†</sup>, Miloš T. Ivanović<sup>1†</sup>, Simone A. Del Grosso<sup>1</sup>, Aritra Chowdhury<sup>1</sup>, Andrea Sottini<sup>1</sup>, Daniel Nettels<sup>1</sup>, Robert B. Best<sup>3†</sup> and Benjamin Schuler<sup>1,2†</sup>

<sup>1</sup>Department of Biochemistry, University of Zurich, Zurich, Switzerland

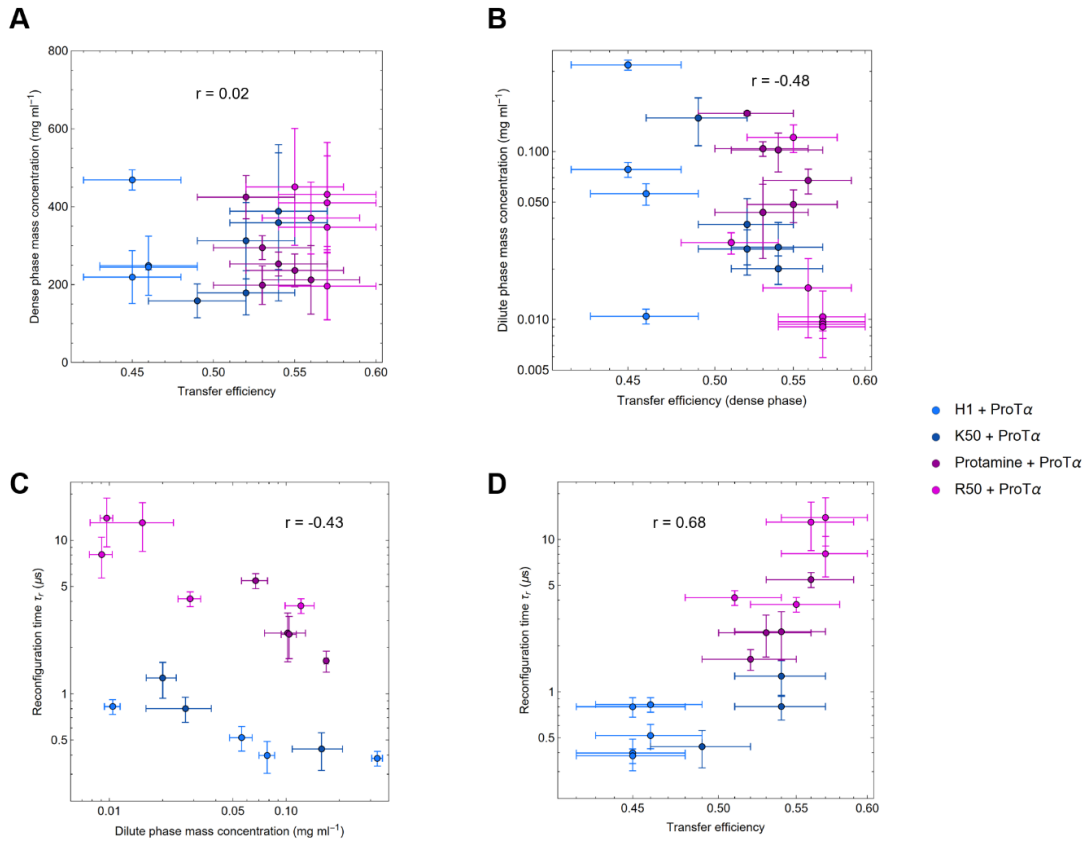
<sup>2</sup>Department of Physics, University of Zurich, Zurich, Switzerland

<sup>3</sup>Laboratory of Chemical Physics, National Institute of Diabetes and Digestive and Kidney Diseases, National Institutes of Health, Bethesda, MD, USA

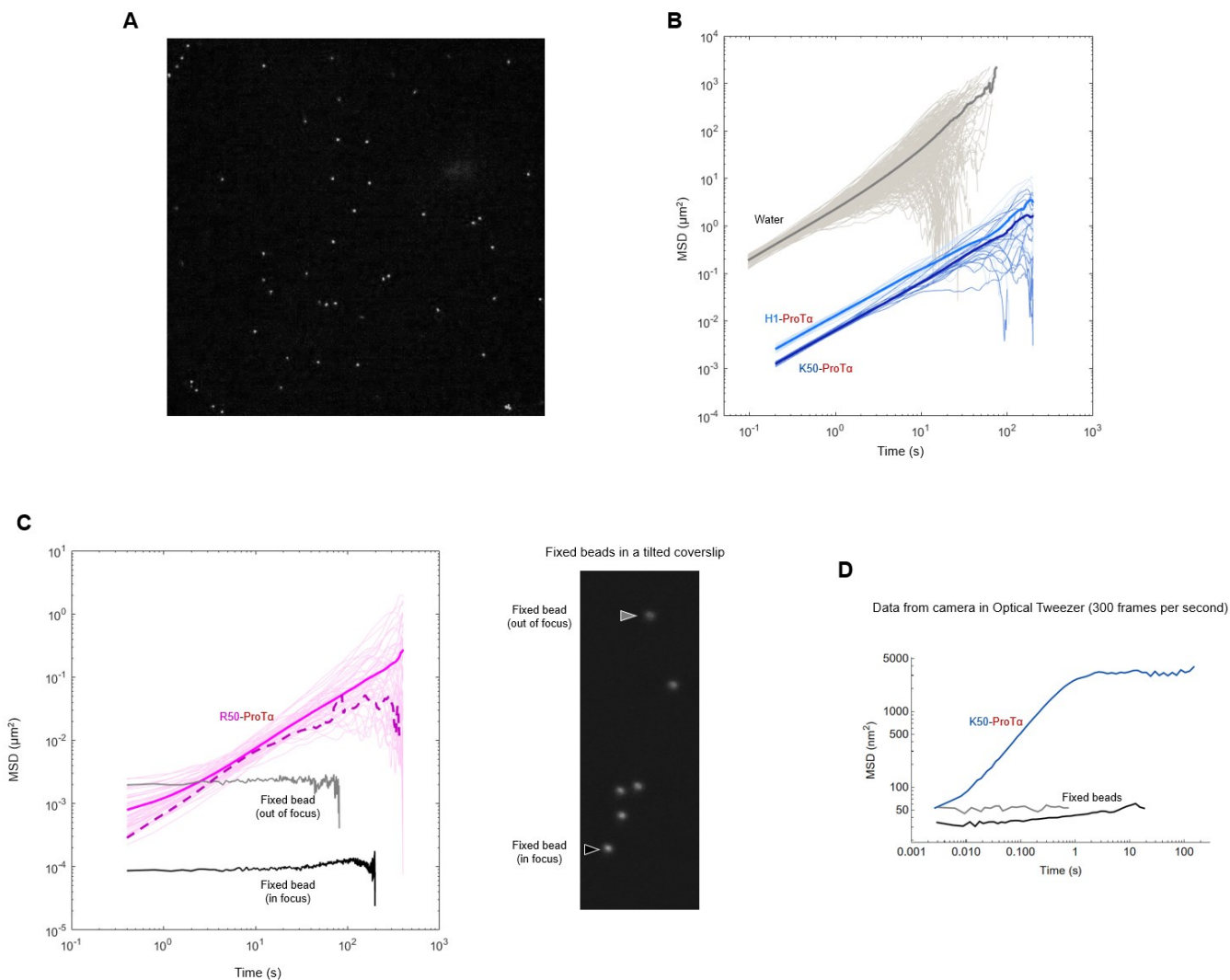
†Corresponding authors: N. Galvanetto ([n.galvanetto@bioc.uzh.ch](mailto:n.galvanetto@bioc.uzh.ch)), M. T. Ivanović ([m.ivanovic@bioc.uzh.ch](mailto:m.ivanovic@bioc.uzh.ch)), R. B. Best ([robert.best2@nih.gov](mailto:robert.best2@nih.gov)), B. Schuler ([schuler@bioc.uzh.ch](mailto:schuler@bioc.uzh.ch))



**Supplementary Fig. 1. Phase separation is most pronounced for protein mixtures near charge balance.** The extent of droplet formation was assessed using turbidity at a constant concentration of 10  $\mu\text{M}$  ProT $\alpha$  and varying amounts of its polycationic partners at 120 mM KCl. Maximal phase separation was observed at a molar ratio  $\lambda$  close to concentration ratios where the charges of the two polymers balance: from left to right,  $\lambda_{\text{H1-ProT}\alpha} \approx 0.8:1$ ,  $\lambda_{\text{K50-ProT}\alpha} \approx 0.9:1$ ,  $\lambda_{\text{protamine-ProT}\alpha} \approx 2:1$ ,  $\lambda_{\text{R50-ProT}\alpha} \approx 0.9:1$ . We note that the arginine-rich samples (protamine and R50) tend to phase-separate even with excess of the polycationic partner, reflecting the complex interactions of arginine beyond Coulomb interactions (42, 43).

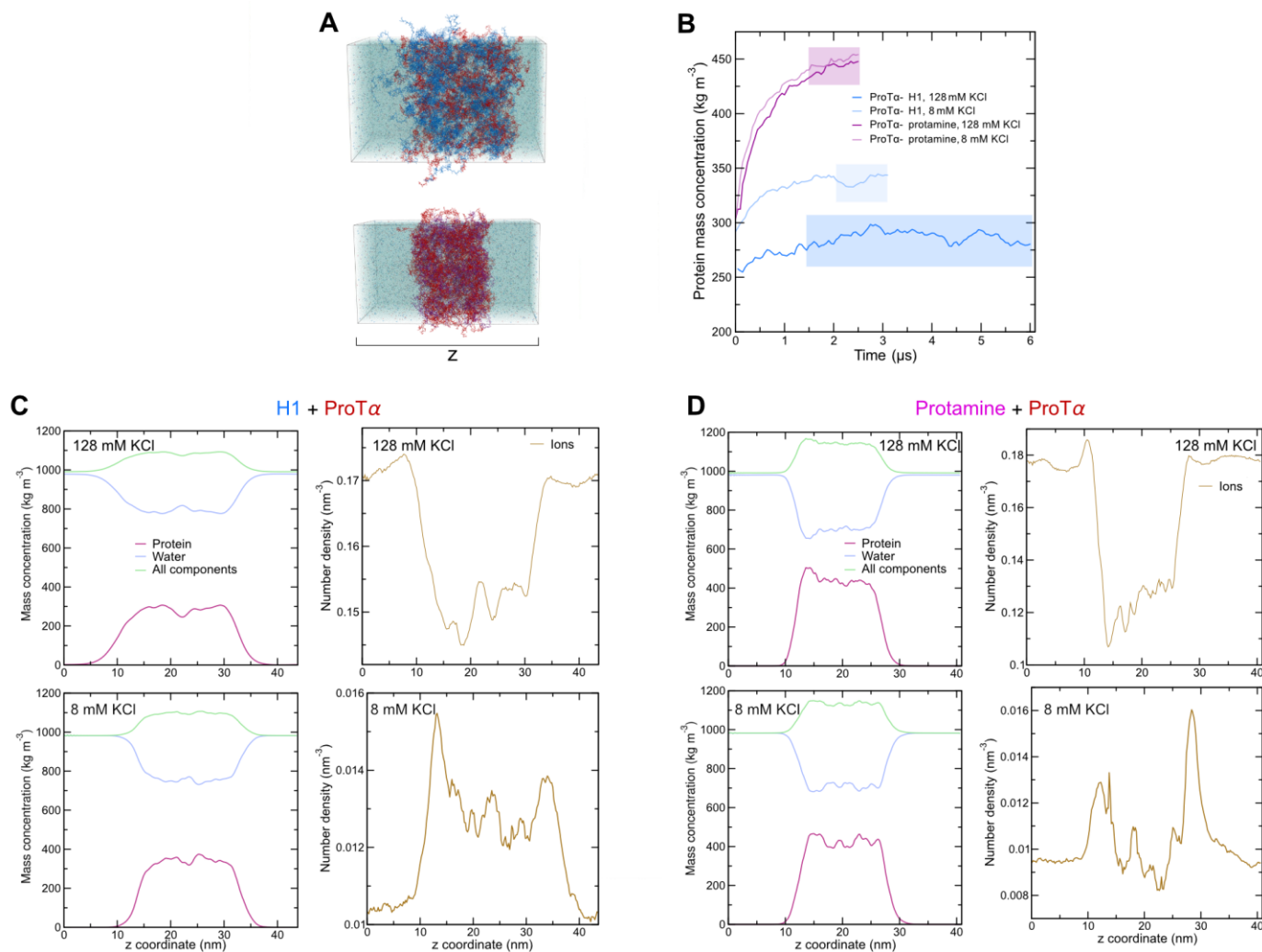


**Supplementary Fig. 2. Correlations between thermodynamic and dynamic quantities in the dense and dilute phases.** (A) ProT $\alpha$  transfer efficiency vs dense phase protein concentration shows no correlation. (B) ProT $\alpha$  transfer efficiency in dense- vs dilute-phase protein concentration shows a slight correlation, indicating that both thermodynamic quantities are proxies for the interaction strength between polymers: the stronger the interaction, the lower the dilute phase concentration and the smaller the chain dimensions (74). (C) Correlations between chain reconfiguration time,  $\tau_r$ , and dilute phase mass concentration, and (D) between  $\tau_r$  and transfer efficiency relate the molecular dynamics within condensates to the intermolecular interactions of the systems as proposed by An *et al.* (29).

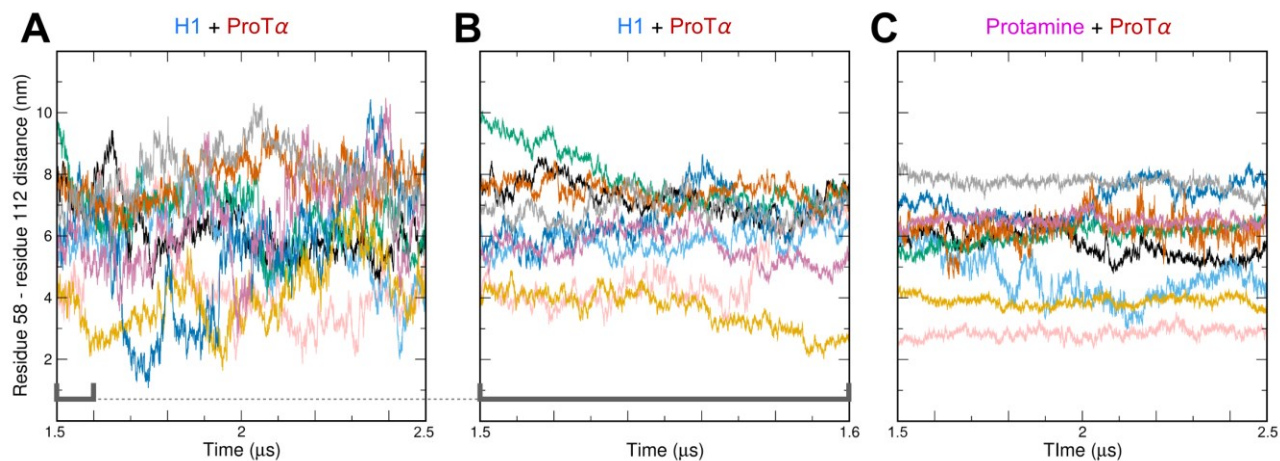


**Supplementary Fig. 3. Passive microrheology shows Brownian diffusion of beads in the dense phase down to the millisecond timescale.** (A) Example of a fluorescence micrograph of 500-nm beads in a K50-ProT $\alpha$  droplet (image size: 150x150  $\mu\text{m}$ ). (B) Mean-squared displacement (MSD) of individual 500-nm beads and their average (solid thick lines) in water, in K50-ProT $\alpha$  dense phase in 60 mM KCl, and in H1-ProT $\alpha$  dense phase in 120 mM KCl show Brownian diffusion. (C) MSD of 500-nm beads in R50-ProT $\alpha$  dense phase in 90 mM KCl (right) apparently deviates from Brownian diffusion at short times, which might be mistaken to suggest the approach of the elastic plateau (72). Further examination of the MSD of beads fixed on a cover slide at different positions relative to the focal plane (left) indicates that this deviation is an artifact due to the limited precision in determining the position of the beads. A stricter threshold for automatic bead identification can reduce this artifact (dashed line), but it also reduces the number and length of individual trajectories, making viscosity determination problematic over longer time periods. (D) MSD of a single polystyrene bead (1  $\mu\text{m}$  diameter) trapped in the dense phase of K50-ProT $\alpha$  with optical tweezers also appears to change slope at short times. Similarly, the deviation which occur for MSD values <100  $\text{nm}^2$  is likely caused by the limited precision in determining the position of the beads. (Tracking was performed from brightfield images taken with maximum LED illumination, see Methods).

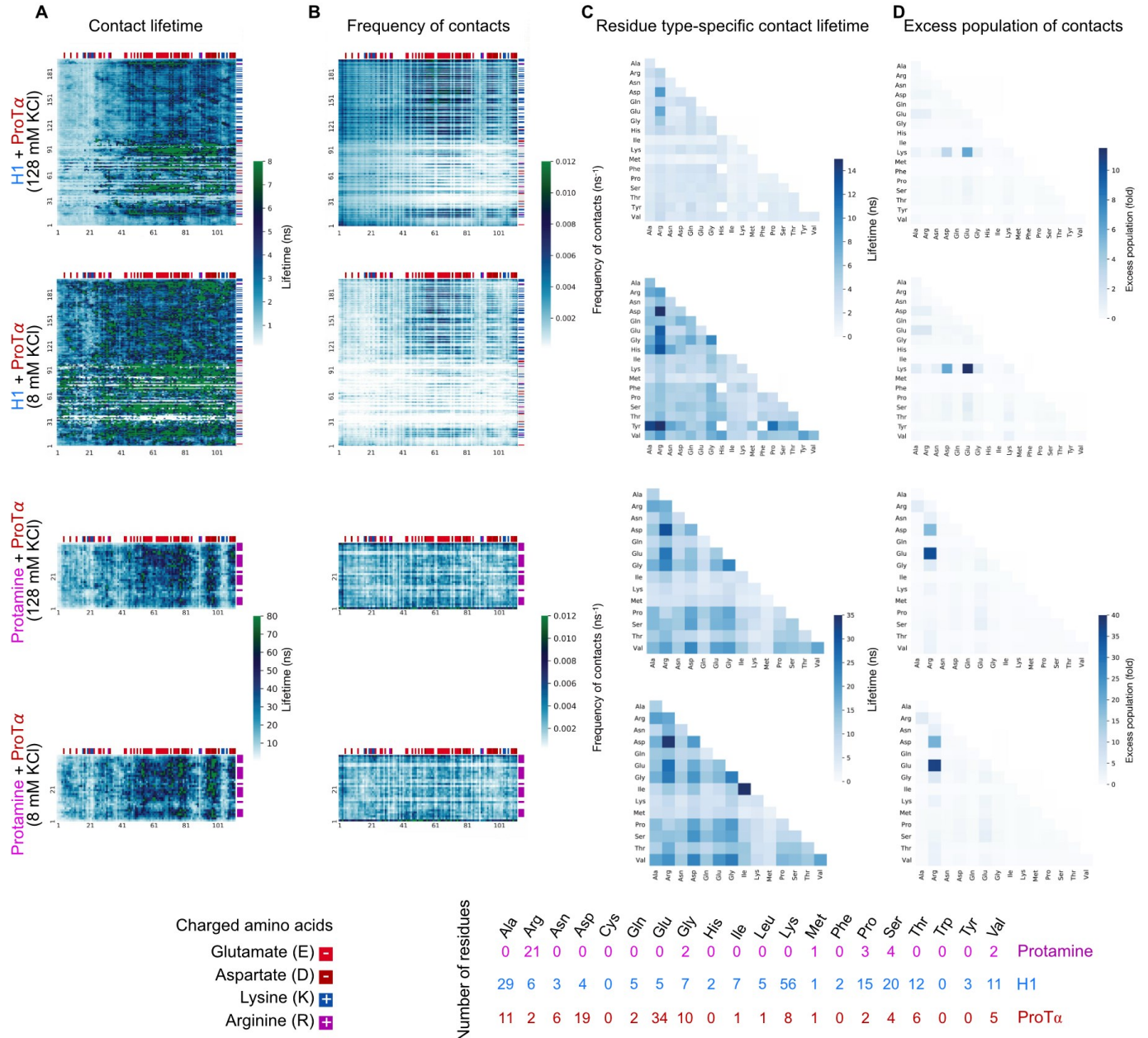




**Supplementary Fig. 4. Mass concentrations and ions distributions in MD simulations.** (A) Illustrations of H1–ProTα and protamine–ProTα simulations in slab geometries. Densities were calculated along the z-axis. (B) Protein density in the dense-phase slabs as a function of time, calculated in 50-ns blocks. The parts of the simulations where the protein density increases significantly with time were treated as equilibration and omitted from the analysis. The parts of the simulations that were analyzed are highlighted by the shaded boxes. (C–D) Mass concentrations of protein, water, all components (protein, water, and ions; left axes), and number density of ions (right axes) along the z-axis of the simulation box in the four different simulations. The water density in the protamine–ProTα simulations is lower compared to the water density in the H1–ProTα simulations, which is consistent with the higher protein density observed in the protamine–ProTα simulations. For the simulations with a total salt concentration of 128 mM KCl, ion concentrations within the dense phase are decreased relative to the dilute phase in both the H1–ProTα and protamine–ProTα simulations, in parallel with the decrease in water content within the dense phases. Conversely, for the simulations with a total salt concentration of 8 mM KCl, ion concentrations are increased in the dense phase relative to the dilute phase in both the H1–ProTα and protamine–ProTα simulations.

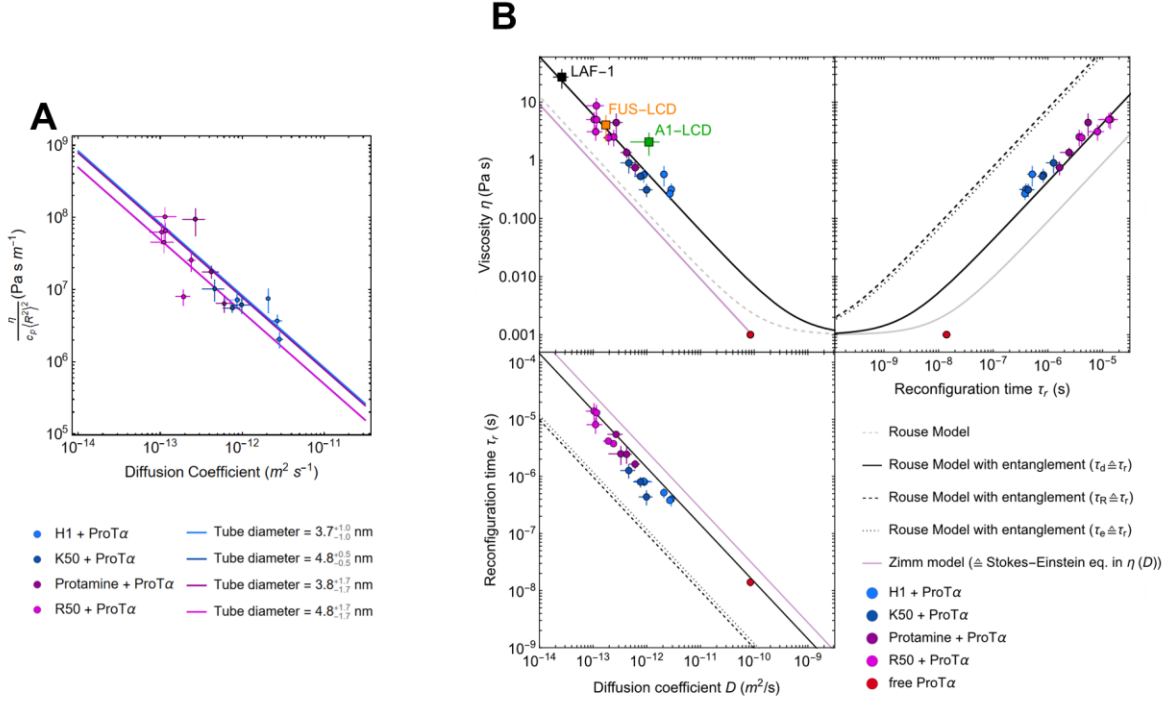


**Supplementary Fig. 5. Comparison of ProT $\alpha$  chain dynamics in H1-ProT $\alpha$  and protamine-ProT $\alpha$  droplets at 128 mM KCl from MD simulations.** (A) Examples of intrachain distance fluctuations between residues 58 and 112 for 9 of the 96 ProT $\alpha$  chains (chain 10, 20, ... , 90) in the H1-ProT $\alpha$  dense phase over 1  $\mu$ s. (B) Same as A, but illustrated for the first 0.1  $\mu$ s. (C) Examples of intrachain distance fluctuations between residues 58 and 112 for 9 of the 96 ProT $\alpha$  chains in the protamine-ProT $\alpha$  dense phase over 1  $\mu$ s are qualitatively comparable to the distance fluctuations in the H1-ProT $\alpha$  slab during 0.1  $\mu$ s, further illustrating the  $\sim$ 10-fold slower chain dynamics in the protamine-ProT $\alpha$  dense phase.

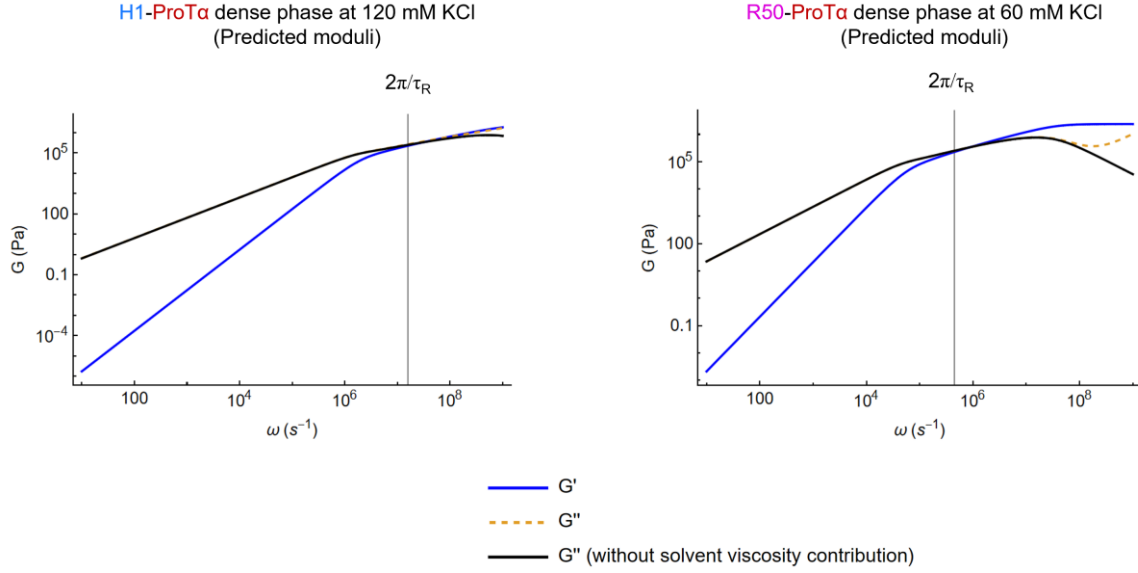


**Supplementary Fig. 6. Contact lifetime heatmaps from MD simulations. (A)** Average lifetime of residue-residue contacts, calculated by considering all instances of these residues across all chains. Numbers on the bottom and left denote the residue numbers of ProTα and H1 or protamine, respectively. Note that H1 contains a folded globular domain (GD) between residues 22 and 96. Bars at the top and right of the plots denote charged residues, as in Figure 1A. **(B)** Frequency of contacts (defined as the number of new contacts made by one ProTα residue per nanosecond). Plots **A** and **B** indicate that: (i) decreasing salt concentration increases the lifetime of residue-residue contacts (see also Figure 3F); (ii) contact times in arginine-rich droplets (Protamine–ProTα) are longer than in lysine-rich droplets (H1–ProTα) (see also Figure 3F); (iii) charge-charge contacts are the most frequent but the most short-lived contacts in the lysine-rich condensates, whereas charge-charge contacts are both the most frequent and the longest-lived in the arginine-rich condensates, reflecting the propensity of arginine to form multivalent contacts (see also Figure 3J). **(C)** Average lifetimes of residue-residue contacts classified by residue type. Residue pairs that are never observed (white squares) and extremely long-lived pairs (dark blue) typically correspond to residue types that are rare in the ProTα and H1/protamine sequences. **(D)** Excess populations of contacts between specific types of residues (determined by dividing the average number of observed contacts for a pair of residue types by the value that would be expected if

residues paired randomly in a mean-field approximation, see Methods). The large excess of contacts between charged residues indicates that their interactions are the most favorable in both lysine- and arginine-rich condensates. Although these contacts are the most frequent, their lifetimes are in the same range as those of other residue pairs (see **C**). In addition, the excess of charged residue interactions is more pronounced in arginine-rich condensates than in lysine-rich condensates, in line with the propensity of arginine to form multivalent contacts (64, 67, 133–135).

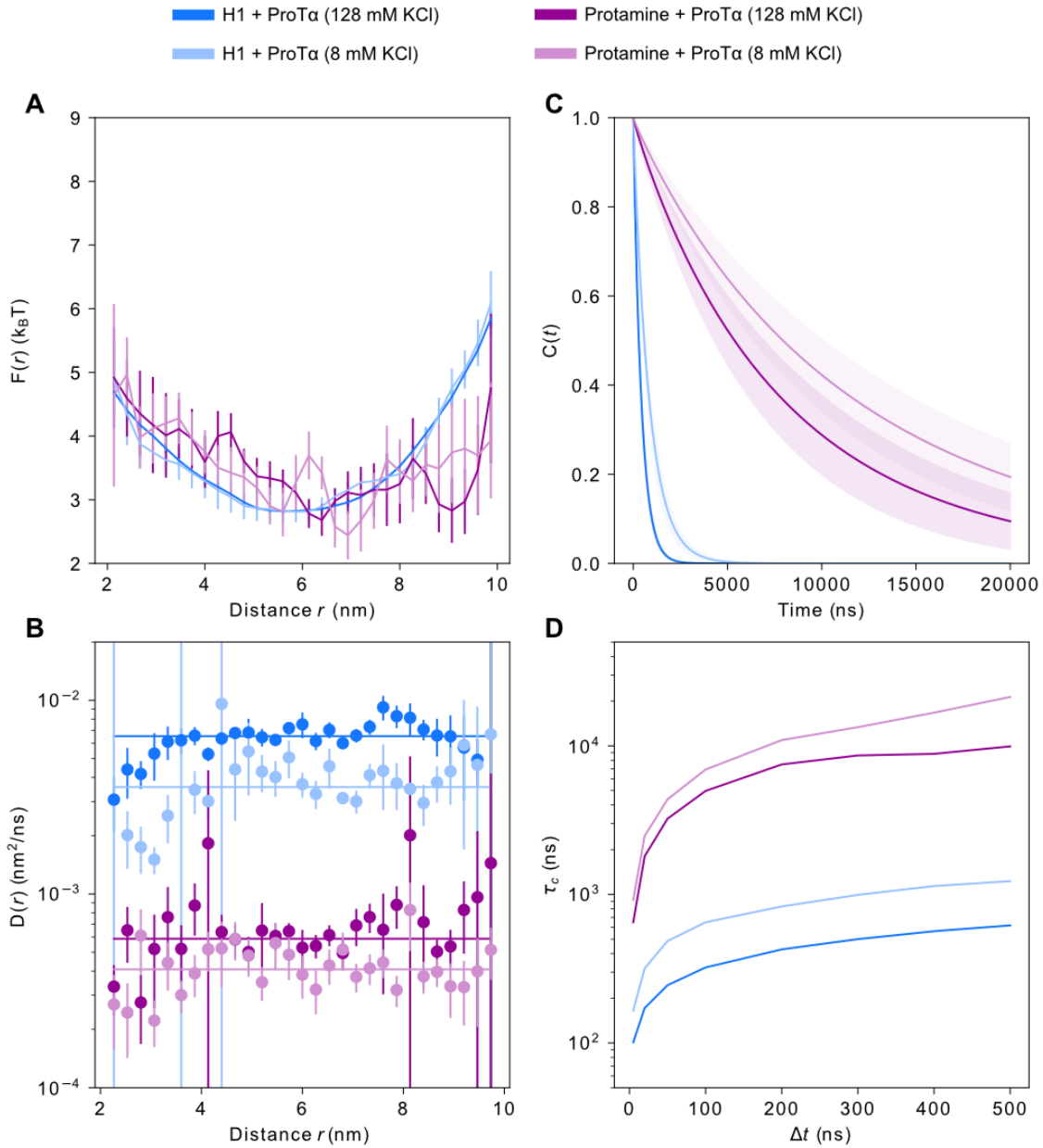


**Supplementary Fig. 7. Comparison of experimental data with different polymer models. (A)** The reduced viscosity  $\frac{\eta}{c_p \langle R^2 \rangle^2}$  allows us to evaluate the relation between viscosity and diffusion coefficient  $D$  (see Eq. 4), taking into account the contribution from the slightly different chain dimensions,  $\langle R^2 \rangle$ , and protein concentrations,  $c_p$ , in the individual samples. The solid lines correspond to the relation  $\frac{\eta}{c_p \langle R^2 \rangle^2} = \frac{k_B T}{36 D} \frac{1}{a^2} + \frac{\eta_s}{c_p \langle R^2 \rangle^2}$ , where the entanglement spacings,  $a$ , were calculated for each individual sample set as  $a = \sqrt{\frac{k_B T c_p \langle R^2 \rangle^2}{36 D \eta}}$ . The means and standard deviations of  $a$  for the individual samples are reported in the legend. For the comparison with other models, we used the average value  $a = 4 \pm 2$  nm. **(B)** Comparison of the experimental viscosity, diffusion coefficient, and chain reconfiguration time with the predictions of the Rouse model, the Zimm model, and the Rouse model with entanglement from Equations 1-5 and 13-21 (see Methods). The viscosities and diffusion coefficients of LAF-1 (54), A1-LCD (73, 74) and FUS-LCD (75, 76) are from previous reports. The average entanglement spacing used in the Rouse model with entanglement is obtained as described in **A** ( $a = 4 \pm 2$  nm). The Rouse model with entanglement predicts three different chain relaxation times:  $\tau_e = \frac{a^6}{3 \langle R^2 \rangle^2 D}$  is the time at which the displacement of chain segments becomes comparable to the entanglement spacing  $a$ ;  $\tau_{\text{tube}} = \frac{a^2}{9 \pi^2 D}$  is the time for chain relaxation within a tube;  $\tau_d = \frac{\langle R^2 \rangle}{3 \pi^2 D}$  is the disentanglement time — the time required for a chain to disentangle from the tube within it was confined. The chain relaxation that best describes the experimental results is  $\tau_d$ , suggesting that the experimentally observed end-to-end distance fluctuations are dominated by chain disentanglement.



**Supplementary Fig. 8. Theoretical storage and loss moduli of the samples with the fastest (left) and slowest (right) chain reconfiguration time,  $\tau_R$ .** The Rouse model (21) can be used to calculate the storage modulus  $G'(\omega) = c_p k_B T \sum_p \frac{\omega^2 \tau_p^2}{1 + \omega^2 \tau_p^2}$  and the loss modulus  $G''(\omega) = \omega \eta_s + c_p k_B T \sum_p \frac{\omega \tau_p}{1 + \omega^2 \tau_p^2}$  of a polymer solution with a concentration of chains,  $c_p$ , and solvent viscosity,  $\eta_s$ , where  $\omega$  is the angular frequency, and  $\tau_p$  is the relaxation time of the  $p$ -th Rouse mode ( $\tau_p = \frac{\tau_R}{p^2}$ , where the longest relaxation mode,  $\tau_1 \triangleq \tau_R$ , is related to the reconfiguration time of the experimentally observed chain segment by the Makarov relation (113),  $\tau_R = \frac{\tau_r}{0.54}$ , see Methods). This theory has previously been shown to accurately describe experimental data on synthetic polymers (136). We note that even in the sample with the slowest reconfiguration time investigated here (R50-ProT $\alpha$  at 60 mM KCl), the predicted crossover frequency,  $\frac{2\pi}{\tau_R}$ , is in the megahertz range, which is difficult to access using conventional rheological methods (18). Similarly, in the case of Rouse theory with entanglement, the crossover frequency is expected to be the inverse of the disentanglement time,  $\tau_d$ , (66, 72) which corresponds to the experimental chain reconfiguration time,  $\tau_r$  (see Supplementary Fig. 7B).





**Supplementary Fig. 9. Computing distance decorrelation times from simulation using a diffusion model.** For each system, the dynamics of the 58-112 distance is modeled using a discretized diffusion model described by (A) free energies,  $F(r)$ , and (B) diffusion coefficients,  $D(r)$ , determined from the molecular simulations. Allowing position-dependent diffusion coefficients (symbols in (B)) shows that constant  $D$  (horizontal lines in (B)) is a good approximation. The model allows properties beyond the  $\sim 1$   $\mu$ s time scale of the equilibrated portion of most of the simulations to be estimated, such as (C) correlation functions and (D) correlation times. Based on the convergence of correlation time,  $\tau_c$ , with lag time,  $\Delta t$ , in (D), a lag time of 200 ns was chosen for all systems and was used in the models for (A)-(C).

ProTα (unlabeled)	GPMSDAAVDTSSSEITTKDLKEKKEVVVEEAENGRDAPANGNANEENGEQEADNEVDEEE EEGGEEEEEEEEEGDGEEDGDEDEEAESATGKRAAEDDEDVDTKKQKTDEDD
ProTαC (56C/110C labeled)	GPSDAAVDTSSSEITTKDLKEKKEVVVEEAENGRDAPANGNAENEENGEQEADNEVDEEC EEGGEEEEEEEEEGDGEEDGDEDEEAESATGKRAAEDDEDVDTKKQKTDEDC
H1 (unlabeled)	TENSTSAPAAKPKRAKASKKSTDHPKYSDMIVAAIQAEKNRAGSSRQSIQKYIKSHYK VGENADSQIKLSIKRLVTTGVLKQTKGVGASGSFRLAKSDEPKKSVAFKKTKEIKKV ATPKKASKPKKAASKAPTCKPKATPVKKAKKKLAATPKKAKPKTKVAKPKVASKPKK AKPVKPKAKSSAKRAGKKK
Protamine (unlabeled)	MPRRRRSSSRPVRRRRRPRVSRRRRRRGRRRR
Poly-L-lysine 50	KK
Poly-L-arginine 50	RR

**Supplementary Table 1.** Amino acid sequences of polypeptides used. Cys residues introduced for labeling are indicated in bold. Unlabeled ProTα is a variant of human ProTα isoform 2, while ProTα 2C/56C is a variant of isoform 1. (57) The isoforms differ by a single Glu at position 39.

**Supplementary Video 1** [\[link\]](#)

**(Left)** All-atom explicit-solvent simulation of the ProTα–H1 condensate (total time 1 μs). One ProTα chain is highlighted in red (chain 60), and four interacting H1 chains are shown in different shades of blue. Other surrounding ProTα and H1 chains are shown semi-transparently in red and blue, respectively.

**(Right)** All-atom explicit-solvent simulation of the ProTα–protamine condensate (total time 1 μs). One ProTα chain is highlighted in red (chain 30), and six interacting protamine chains are shown in three different shades of purple. Other surrounding ProTα and protamine chains are shown semi-transparently in red and purple, respectively.

Both videos are centered on the center of mass of the highlighted ProTα chain. The video is shown at 2 ns per frame. To slightly smooth the motion, a filter with a time constant of 4 ns was applied to all frames. Protein hydrogen atoms, water molecules, and ions were omitted for clarity.

(YouTube link: [https://www.youtube.com/watch?v=E4Idah1J3N8&ab\\_channel=MilosIvanovic](https://www.youtube.com/watch?v=E4Idah1J3N8&ab_channel=MilosIvanovic))

**Supplementary Video 2** [\[link\]](#)

**(Left)** All-atom explicit-solvent simulation of the ProTα–H1 condensate (total time 50 ns). One ProTα chain is highlighted in red (chain 59), and four interacting H1 chains are shown in different shades of blue. Other surrounding ProTα and H1 chains are shown semi-transparently in red and blue, respectively.

**(Right)** All-atom explicit-solvent simulation of the ProTα–protamine condensate (total time 50 ns). One ProTα chain is highlighted in red (chain 30), and six interacting protamine chains are shown in three different shades of purple. Other surrounding ProTα and protamine chains are shown semi-transparently in red and purple, respectively.

Both videos are centered on the center of mass of the highlighted ProTα chain. The video is shown at 100 ps per frame. To slightly smooth the motion, a filter with a time constant of 200 ps was applied to all frames. Protein hydrogen atoms, water molecules, and ions were omitted for clarity.

(YouTube link: [https://www.youtube.com/watch?v=4G9GOYp-Fmw&ab\\_channel=MilosIvanovic](https://www.youtube.com/watch?v=4G9GOYp-Fmw&ab_channel=MilosIvanovic))

## References

1. Keber, F.C., T. Nguyen, A. Mariossi, C.P. Brangwynne, and M. Wühr. 2024. Evidence for widespread cytoplasmic structuring into mesoscale condensates. *Nat Cell Biol.* 1–7.
2. Brangwynne, C.P., P. Tompa, and R.V. Pappu. 2015. Polymer physics of intracellular phase transitions. *Nature Physics.* 11:899–904.
3. Hyman, A.A., C.A. Weber, and F. Jülicher. 2014. Liquid-Liquid Phase Separation in Biology. *Annual Review of Cell and Developmental Biology.* 30:39–58.
4. Zhou, H.-X., D. Kota, S. Qin, and R. Prasad. 2024. Fundamental Aspects of Phase-Separated Biomolecular Condensates. *Chem. Rev.*
5. Espinosa, J.R., J.A. Joseph, I. Sanchez-Burgos, A. Garaizar, D. Frenkel, and R. Collepardo-Guevara. 2020. Liquid network connectivity regulates the stability and composition of biomolecular condensates with many components. *Proceedings of the National Academy of Sciences.* 117:13238–13247.
6. Gibbs, E.B., and R.W. Kriwacki. 2018. Linker histones as liquid-like glue for chromatin. *Proceedings of the National Academy of Sciences.* 115:11868–11870.
7. Gibson, B.A., L.K. Doolittle, M.W.G. Schneider, L.E. Jensen, N. Gamarra, L. Henry, D.W. Gerlich, S. Redding, and M.K. Rosen. 2019. Organization of Chromatin by Intrinsic and Regulated Phase Separation. *Cell.* 179:470–484.e21.
8. Lyon, A.S., W.B. Peeples, and M.K. Rosen. 2021. A framework for understanding the functions of biomolecular condensates across scales. *Nat Rev Mol Cell Biol.* 22:215–235.
9. Alberti, S., A. Gladfelter, and T. Mittag. 2019. Considerations and Challenges in Studying Liquid-Liquid Phase Separation and Biomolecular Condensates. *Cell.* 176:419–434.
10. Dignon, G.L., R.B. Best, and J. Mittal. 2020. Biomolecular Phase Separation: From Molecular Driving Forces to Macroscopic Properties. *Annual Review of Physical Chemistry.* 71:53–75.
11. Mukherjee, S., and L.V. Schäfer. 2023. Thermodynamic forces from protein and water govern condensate formation of an intrinsically disordered protein domain. *Nat Commun.* 14:5892.
12. Priftis, D., and M. Tirrell. 2012. Phase behaviour and complex coacervation of aqueous polypeptide solutions. *Soft Matter.* 8:9396–9405.
13. Küffner, A.M., M. Prodan, R. Zuccarini, U. Capasso Palmiero, L. Faltova, and P. Arosio. 2020. Acceleration of an Enzymatic Reaction in Liquid Phase Separated Compartments Based on Intrinsically Disordered Protein Domains. *ChemSystemsChem.* 2:e2000001.
14. Nakashima, K.K., M.A. Vibhute, and E. Spruijt. 2019. Biomolecular Chemistry in Liquid Phase Separated Compartments. *Frontiers in Molecular Biosciences.* 6.
15. Hubatsch, L., L.M. Jawerth, C. Love, J. Bauermann, T.D. Tang, S. Bo, A.A. Hyman, and C.A. Weber. 2021. Quantitative theory for the diffusive dynamics of liquid condensates. *eLife.* 10:e68620.
16. Peeples, W., and M.K. Rosen. 2021. Mechanistic dissection of increased enzymatic rate in a phase-separated compartment. *Nat Chem Biol.* 17:693–702.
17. Stroberg, W., and S. Schnell. 2018. Do Cellular Condensates Accelerate Biochemical Reactions? Lessons from Microdroplet Chemistry. *Biophysical Journal.* 115:3–8.
18. Alshareedah, I., T. Kaur, and P.R. Banerjee. 2021. Chapter Six - Methods for characterizing the material properties of biomolecular condensates. In: Keating CD, editor. *Methods in Enzymology.* Academic Press. pp. 143–183.
19. Bussi, C., A. Mangiarotti, C. Vanhille-Campos, B. Aylan, E. Pellegrino, N. Athanasiadi, A. Fearn, A. Rodgers, T.M. Franzmann, A. Šarić, R. Dimova, and M.G. Gutierrez. 2023. Stress granules plug and stabilize damaged endolysosomal membranes. *Nature.* 623:1062–1069.
20. Lasker, K., S. Boeynaems, V. Lam, D. Scholl, E. Stainton, A. Briner, M. Jacquemyn, D. Daelemans, A. Deniz, E. Villa, A.S. Holehouse, A.D. Gitler, and L. Shapiro. 2022. The material properties of a bacterial-derived biomolecular condensate tune biological function in natural and synthetic systems. *Nat Commun.* 13:5643.
21. Rouse, P.E. 1953. A Theory of the Linear Viscoelastic Properties of Dilute Solutions of Coiling Polymers. *The Journal of Chemical Physics.* 21:1272–1280.
22. Rubinstein, M., and R.H. Colby. 2003. *Polymer Physics.* OUP Oxford.
23. Alshareedah, I., M.M. Moosa, M. Pham, D.A. Potoyan, and P.R. Banerjee. 2021. Programmable viscoelasticity in protein-RNA condensates with disordered sticker-spacer polypeptides. *Nat Commun.* 12:1–14.
24. Dai, Y., M. Farag, D. Lee, X. Zeng, K. Kim, H. Son, X. Guo, J. Su, N. Peterson, J. Mohammed, M. Ney, D.M. Shapiro, R.V. Pappu, A. Chilkoti, and L. You. 2023. Programmable synthetic biomolecular condensates for cellular control. *Nat Chem Biol.* 1–11.
25. Do, S., C. Lee, T. Lee, D.-N. Kim, and Y. Shin. 2022. Engineering DNA-based synthetic condensates with programmable material properties, compositions, and functionalities. *Science Advances.* 8:eabj1771.
26. Hazra, M.K., and Y. Levy. 2020. Charge pattern affects the structure and dynamics of polyampholyte condensates. *Phys. Chem. Chem. Phys.* 22:19368–19375.

27. Rekhi, S., C.G. Garcia, M. Barai, A. Rizuan, B.S. Schuster, K.L. Kiick, and J. Mittal. 2024. Expanding the molecular language of protein liquid–liquid phase separation. *Nat. Chem.* 1–12.
28. Sundaravadeivelu Devarajan, D., J. Wang, B. Szała-Mendyk, S. Rekhi, A. Nikoubashman, Y.C. Kim, and J. Mittal. 2024. Sequence-dependent material properties of biomolecular condensates and their relation to dilute phase conformations. *Nat Commun.* 15:1912.
29. An, Y., M.A. Webb, and W.M. Jacobs. 2024. Active learning of the thermodynamics-dynamics trade-off in protein condensates. *Science Advances.* 10:eadj2448.
30. Strom, A.R., A.V. Emelyanov, M. Mir, D.V. Fyodorov, X. Darzacq, and G.H. Karpen. 2017. Phase separation drives heterochromatin domain formation. *Nature.* 547:241–245.
31. King, M.R., K.M. Ruff, A.Z. Lin, A. Pant, M. Farag, J.M. Lalmansingh, T. Wu, M.J. Fossat, W. Ouyang, M.D. Lew, E. Lundberg, M.D. Vahey, and R.V. Pappu. 2024. Macromolecular condensation organizes nucleolar sub-phases to set up a pH gradient. *Cell.* 187:1889–1906.e24.
32. Alberts, B. 2022. *Molecular Biology of the Cell.* New York, NY London: .
33. Ferrara, D., G. Izzo, L. Liguori, M. d'Istria, F. Aniello, and S. Minucci. 2009. Evidence for the involvement of prothymosin  $\alpha$  in the spermatogenesis of the frog *Rana esculenta*. *Journal of Experimental Zoology Part A: Ecological Genetics and Physiology.* 311A:1–10.
34. Heidarsson, P.O., D. Mercadante, A. Sottini, D. Nettels, M.B. Borgia, A. Borgia, S. Kilic, B. Fierz, R.B. Best, and B. Schuler. 2022. Release of linker histone from the nucleosome driven by polyelectrolyte competition with a disordered protein. *Nat. Chem.* 14:224–231.
35. Sarandeses, C.S., G. Covelo, C. Díaz-Jullien, and M. Freire. 2003. Prothymosin  $\alpha$  Is Processed to Thymosin  $\alpha$ 1 and Thymosin  $\alpha$ 11 by a Lysosomal Asparaginyl Endopeptidase\*. *Journal of Biological Chemistry.* 278:13286–13293.
36. Galvanetto, N., M.T. Ivanović, A. Chowdhury, A. Sottini, M.F. Nüesch, D. Nettels, R.B. Best, and B. Schuler. 2023. Extreme dynamics in a biomolecular condensate. *Nature.* 619:876–883.
37. Rumyantsev, A.M., N.E. Jackson, and J.J. de Pablo. 2021. Polyelectrolyte Complex Coacervates: Recent Developments and New Frontiers. *Annu. Rev. Condens. Matter Phys.* 12:155–176.
38. Srivastava, S., and M.V. Tirrell. 2016. Polyelectrolyte Complexation. In: *Advances in Chemical Physics.* John Wiley & Sons, Ltd. pp. 499–544.
39. Fisher, R.S., and S. Elbaum-Garfinkle. 2020. Tunable multiphase dynamics of arginine and lysine liquid condensates. *Nature Communications.* 11.
40. Kim, S., M. Lee, W.B. Lee, and S.-H. Choi. 2021. Ionic-Group Dependence of Polyelectrolyte Coacervate Phase Behavior. *Macromolecules.*
41. Lin, Y., J. McCarty, J.N. Rauch, K.T. Delaney, K.S. Kosik, G.H. Fredrickson, J.-E. Shea, and S. Han. 2019. Narrow equilibrium window for complex coacervation of tau and RNA under cellular conditions. *eLife.* 8:e42571.
42. Kim, S., J. Huang, Y. Lee, S. Dutta, H.Y. Yoo, Y.M. Jung, Y. Jho, H. Zeng, and D.S. Hwang. 2016. Complexation and coacervation of like-charged polyelectrolytes inspired by mussels. *Proceedings of the National Academy of Sciences.* 113:E847–E853.
43. Hong, Y., S. Najafi, T. Casey, J.-E. Shea, S.-I. Han, and D.S. Hwang. 2022. Hydrophobicity of arginine leads to reentrant liquid-liquid phase separation behaviors of arginine-rich proteins. *Nat Commun.* 13:7326.
44. Sing, C.E., and S.L. Perry. 2020. Recent progress in the science of complex coacervation. *Soft Matter.* 16:2885–2914.
45. Spruijt, E., A.H. Westphal, J.W. Borst, M.A. Cohen Stuart, and J. van der Gucht. 2010. Binodal Compositions of Polyelectrolyte Complexes. *Macromolecules.* 43:6476–6484.
46. Krainer, G., T.J. Welsh, J.A. Joseph, J.R. Espinosa, S. Wittmann, E. de Csilléry, A. Sridhar, Z. Toprakcioglu, G. Gudiškytė, M.A. Czekalska, W.E. Arter, J. Guillén-Boixet, T.M. Franzmann, S. Qamar, P.S. George-Hyslop, A.A. Hyman, R. Collepardo-Guevara, S. Alberti, and T.P.J. Knowles. 2021. Reentrant liquid condensate phase of proteins is stabilized by hydrophobic and non-ionic interactions. *Nat Commun.* 12:1085.
47. Kumar, K., S.M. Woo, T. Siu, W.A. Cortopassi, F. Duarte, and R.S. Paton. 2018. Cation- $\pi$  interactions in protein–ligand binding: theory and data-mining reveal different roles for lysine and arginine. *Chem. Sci.* 9:2655–2665.
48. Petrauskas, V., E. Maximowitsch, and D. Matulis. 2015. Thermodynamics of Ion Pair Formations Between Charged Poly(Amino Acid)s. *J. Phys. Chem. B.* 119:12164–12171.
49. Millefiori, S., A. Alparone, A. Millefiori, and A. Vanella. 2008. Electronic and vibrational polarizabilities of the twenty naturally occurring amino acids. *Biophysical Chemistry.* 132:139–147.
50. Chowdhury, A., A. Borgia, S. Ghosh, A. Sottini, S. Mitra, R.S. Eapen, M.B. Borgia, T. Yang, N. Galvanetto, M.T. Ivanović, P. Łukijańczuk, R. Zhu, D. Nettels, A. Kundagrami, and B. Schuler. 2023. Driving forces of the complex formation between highly charged disordered proteins. *Proceedings of the National Academy of Sciences.* 120:e2304036120.
51. Müller-Späth, S., A. Soranno, V. Hirschfeld, H. Hofmann, S. Rügger, L. Reymond, D. Nettels, and B. Schuler. 2010. Charge interactions can dominate the dimensions of intrinsically disordered proteins. *Proceedings of the National Academy of Sciences.* 107:14609–14614.

52. Nettels, D., I.V. Gopich, A. Hoffmann, and B. Schuler. 2007. Ultrafast dynamics of protein collapse from single-molecule photon statistics. *Proceedings of the National Academy of Sciences*. 104:2655–2660.
53. Schuler, B., A. Soranno, H. Hofmann, and D. Nettels. 2016. Single-Molecule FRET Spectroscopy and the Polymer Physics of Unfolded and Intrinsically Disordered Proteins. *Annual Review of Biophysics*. 45:207–231.
54. Wei, M.-T., S. Elbaum-Garfinkle, A.S. Holehouse, C.C.-H. Chen, M. Feric, C.B. Arnold, R.D. Priestley, R.V. Pappu, and C.P. Brangwynne. 2017. Phase behaviour of disordered proteins underlying low density and high permeability of liquid organelles. *Nature Chemistry*. 9:1118–1125.
55. Zheng, W., G.L. Dignon, N. Jovic, X. Xu, R.M. Regy, N.L. Fawzi, Y.C. Kim, R.B. Best, and J. Mittal. 2020. Molecular Details of Protein Condensates Probed by Microsecond Long Atomistic Simulations. *J. Phys. Chem. B*. 124:11671–11679.
56. Farag, M., S.R. Cohen, W.M. Borchers, A. Bremer, T. Mittag, and R.V. Pappu. 2022. Condensates formed by prion-like low-complexity domains have small-world network structures and interfaces defined by expanded conformations. *Nat Commun*. 13:7722.
57. Borgia, A., M.B. Borgia, K. Bugge, V.M. Kissling, P.O. Heidarsson, C.B. Fernandes, A. Sottini, A. Soranno, K.J. Buholzer, D. Nettels, B.B. Kragelund, R.B. Best, and B. Schuler. 2018. Extreme disorder in an ultrahigh-affinity protein complex. *Nature*. 555:61–66.
58. Armstrong, C.T., P.E. Mason, J.L.R. Anderson, and C.E. Dempsey. 2016. Arginine side chain interactions and the role of arginine as a gating charge carrier in voltage sensitive ion channels. *Sci Rep*. 6:21759.
59. Mason, P.E., G.W. Neilson, C.E. Dempsey, A.C. Barnes, and J.M. Cruickshank. 2003. The hydration structure of guanidinium and thiocyanate ions: Implications for protein stability in aqueous solution. *Proceedings of the National Academy of Sciences*. 100:4557–4561.
60. Baker, C.M. 2015. Polarizable force fields for molecular dynamics simulations of biomolecules. *WIREs Computational Molecular Science*. 5:241–254.
61. Ronceray, P., Y. Zhang, X. Liu, and N.S. Wingreen. 2022. Stoichiometry Controls the Dynamics of Liquid Condensates of Associative Proteins. *Phys. Rev. Lett*. 128:038102.
62. Xiang, Y.-X., Y. Shan, Q.-L. Lei, C.-L. Ren, and Y.-Q. Ma. 2022. Dynamics of protein condensates in weak-binding regime. *Phys. Rev. E*. 106:044403.
63. Rubinstein, M., and A. Dobrynin. 1997. Solutions of Associative Polymers. *Trends in Polymer Science*. 5:181–186.
64. Wang, J., J.-M. Choi, A.S. Holehouse, H.O. Lee, X. Zhang, M. Jahnel, S. Maharana, R. Lemaitre, A. Pozniakovskiy, D. Drechsel, I. Poser, R.V. Pappu, S. Alberti, and A.A. Hyman. 2018. A Molecular Grammar Governing the Driving Forces for Phase Separation of Prion-like RNA Binding Proteins. *Cell*. 174:688-699.e16.
65. Rubinstein, M., and A.N. Semenov. 2001. Dynamics of Entangled Solutions of Associating Polymers. *Macromolecules*. 34:1058–1068.
66. Doi, M., and S.F. Edwards. 1994. *The Theory of Polymer Dynamics*. Clarendon Press.
67. Paloni, M., G. Bussi, and A. Barducci. 2021. Arginine multivalency stabilizes protein/RNA condensates. *Protein Science*. 30:1418–1426.
68. Fetters, L.J., D.J. Lohse, D. Richter, T.A. Witten, and A. Zirkel. 1994. Connection between Polymer Molecular Weight, Density, Chain Dimensions, and Melt Viscoelastic Properties. *Macromolecules*. 27:4639–4647.
69. De Gennes, P.G. 1976. Dynamics of Entangled Polymer Solutions. I. The Rouse Model. *Macromolecules*. 9:587–593.
70. de Gennes, P.G. 1971. Reptation of a Polymer Chain in the Presence of Fixed Obstacles. *The Journal of Chemical Physics*. 55:572–579.
71. Harmandaris, V.A., V.G. Mavrantzas, D.N. Theodorou, M. Kröger, J. Ramírez, H.C. Öttinger, and D. Vlassopoulos. 2003. Crossover from the Rouse to the Entangled Polymer Melt Regime: Signals from Long, Detailed Atomistic Molecular Dynamics Simulations, Supported by Rheological Experiments. *Macromolecules*. 36:1376–1387.
72. Cai, L.-H., S. Panyukov, and M. Rubinstein. 2011. Mobility of Nonsticky Nanoparticles in Polymer Liquids. *Macromolecules*. 44:7853–7863.
73. Alshareedah, I., W.M. Borchers, S.R. Cohen, A. Singh, A.E. Posey, M. Farag, A. Bremer, G.W. Strout, D.T. Tomares, R.V. Pappu, T. Mittag, and P.R. Banerjee. 2024. Sequence-specific interactions determine viscoelasticity and ageing dynamics of protein condensates. *Nat. Phys.* 1–10.
74. Martin, E.W., A.S. Holehouse, I. Peran, M. Farag, J.J. Incicco, A. Bremer, C.R. Grace, A. Soranno, R.V. Pappu, and T. Mittag. 2020. Valence and patterning of aromatic residues determine the phase behavior of prion-like domains. *Science*. 367:694–699.
75. Ji, C., E. Girardi, N. Fawzi, and J. Tang. 2019. Density and viscosity measurements on the liquid condensates of FUS protein low-complexity domain. *APS March Meeting*. 64:K65.00005.
76. Murthy, A.C., G.L. Dignon, Y. Kan, G.H. Zerze, S.H. Parekh, J. Mittal, and N.L. Fawzi. 2019. Molecular interactions underlying liquid–liquid phase separation of the FUS low-complexity domain. *Nat Struct Mol Biol*. 26:637–648.

77. Akkaoui, K., Z.A. Digby, C. Do, and J.B. Schlenoff. 2024. Comprehensive Dynamics in a Polyelectrolyte Complex Coacervate. *Macromolecules*. acs.macromol.3c01540.
78. Tejedor, A.R., I. Sanchez-Burgos, M. Estevez-Espinosa, A. Garaizar, R. Collepardo-Guevara, J. Ramirez, and J.R. Espinosa. 2022. Protein structural transitions critically transform the network connectivity and viscoelasticity of RNA-binding protein condensates but RNA can prevent it. *Nat Commun*. 13:5717.
79. Mukherjee, S., and L.V. Schäfer. 2024. Heterogeneous Slowdown of Dynamics in the Condensate of an Intrinsically Disordered Protein. 2024.07.15.603508.
80. Zhou, H.-X. 2021. Shape recovery of deformed biomolecular droplets: Dependence on condensate viscoelasticity. *The Journal of Chemical Physics*. 155:145102.
81. Sigler, P.B. 1988. Acid blobs and negative noodles. *Nature*. 333:210–212.
82. Bergeron-Sandoval, L.-P., S. Kumar, H.K. Heris, C.L.A. Chang, C.E. Cornell, S.L. Keller, P. François, A.G. Hendricks, A.J. Ehrlicher, R.V. Pappu, and S.W. Michnick. 2021. Endocytic proteins with prion-like domains form viscoelastic condensates that enable membrane remodeling. *Proceedings of the National Academy of Sciences*. 118:e2113789118.
83. Ghosh, A., D. Kota, and H.-X. Zhou. 2021. Shear relaxation governs fusion dynamics of biomolecular condensates. *Nat Commun*. 12:5995.
84. Jawerth, L., E. Fischer-Friedrich, S. Saha, J. Wang, T. Franzmann, X. Zhang, J. Sachweh, M. Ruer, M. Ijavi, S. Saha, J. Mahamid, A.A. Hyman, and F. Jülicher. 2020. Protein condensates as aging Maxwell fluids. *Science*. 370:1317–1323.
85. Franosch, T., M. Grimm, M. Belushkin, F.M. Mor, G. Foffi, L. Forró, and S. Jeney. 2011. Resonances arising from hydrodynamic memory in Brownian motion. *Nature*. 478:85–88.
86. Cai, P.C., B.A. Krajina, and A.J. Spakowitz. 2020. Brachiation of a polymer chain in the presence of a dynamic network. *Phys. Rev. E*. 102:020501.
87. Perry, S.L., L. Leon, K.Q. Hoffmann, M.J. Kade, D. Priftis, K.A. Black, D. Wong, R.A. Klein, C.F. Pierce, K.O. Margossian, J.K. Whitmer, J. Qin, J.J. de Pablo, and M. Tirrell. 2015. Chirality-selected phase behaviour in ionic polypeptide complexes. *Nat Commun*. 6:6052.
88. Linsenmeier, M., L. Faltova, C. Morelli, U. Capasso Palmiero, C. Seiffert, A.M. Küffner, D. Pinotsi, J. Zhou, R. Mezzenga, and P. Arosio. 2023. The interface of condensates of the hnRNPA1 low-complexity domain promotes formation of amyloid fibrils. *Nat. Chem*. 15:1340–1349.
89. Shen, Y., A. Chen, W. Wang, Y. Shen, F.S. Ruggeri, S. Aime, Z. Wang, S. Qamar, J.R. Espinosa, A. Garaizar, P. St George-Hyslop, R. Collepardo-Guevara, D.A. Weitz, D. Vigolo, and T.P.J. Knowles. 2023. The liquid-to-solid transition of FUS is promoted by the condensate surface. *Proceedings of the National Academy of Sciences*. 120:e2301366120.
90. Wróbel, J.K., R. Cortez, and L. Fauci. 2014. Modeling viscoelastic networks in Stokes flow. *Physics of Fluids*. 26:113102.
91. Biswas, S., and D.A. Potoyan. 2024. Molecular Drivers of Aging in Biomolecular Condensates: Desolvation, Rigidification, and Sticker Lifetimes. *PRX Life*. 2:023011.
92. Tejedor, A.R., R. Collepardo-Guevara, J. Ramirez, and J.R. Espinosa. 2023. Time-Dependent Material Properties of Aging Biomolecular Condensates from Different Viscoelasticity Measurements in Molecular Dynamics Simulations. *J. Phys. Chem. B*. 127:4441–4459.
93. Cohen, S.R., P.R. Banerjee, and R.V. Pappu. 2024. Direct computations of viscoelastic moduli of biomolecular condensates. *The Journal of Chemical Physics*. 161:095103.
94. Makarov, D.E., and H. Hofmann. 2021. Does Electric Friction Matter in Living Cells? *J. Phys. Chem. B*.
95. Sottini, A., A. Borgia, M.B. Borgia, K. Bugge, D. Nettels, A. Chowdhury, P.O. Heidarsson, F. Zosel, R.B. Best, B.B. Kragelund, and B. Schuler. 2020. Polyelectrolyte interactions enable rapid association and dissociation in high-affinity disordered protein complexes. *Nature Communications*. 11:5736.
96. Hellenkamp, B., S. Schmid, O. Doroshenko, O. Opanasyuk, R. Kühnemuth, S. Rezaei Adariani, B. Ambrose, M. Aznauryan, A. Barth, V. Birkedal, M.E. Bowen, H. Chen, T. Cordes, T. Eilert, C. Fijen, C. Gebhardt, M. Götz, G. Gouridis, E. Gratton, T. Ha, P. Hao, C.A. Hanke, A. Hartmann, J. Hendrix, L.L. Hildebrandt, V. Hirschfeld, J. Hohlbein, B. Hua, C.G. Hübner, E. Kallis, A.N. Kapanidis, J.-Y. Kim, G. Krainer, D.C. Lamb, N.K. Lee, E.A. Lemke, B. Levesque, M. Levitus, J.J. McCann, N. Naredi-Rainer, D. Nettels, T. Ngo, R. Qiu, N.C. Robb, C. Röcker, H. Sanabria, M. Schlierf, T. Schröder, B. Schuler, H. Seidel, L. Streit, J. Thurn, P. Tinnefeld, S. Tyagi, N. Vandenberk, A.M. Vera, K.R. Weninger, B. Wunsch, I.S. Yanez-Orozco, J. Michaelis, C.A.M. Seidel, T.D. Craggs, and T. Hugel. 2018. Precision and accuracy of single-molecule FRET measurements—a multi-laboratory benchmark study. *Nat Methods*. 15:669–676.
97. Schuler, B. 2006. Application of Single Molecule Förster Resonance Energy Transfer to Protein Folding. In: Bai Y, R Nussinov, editors. Protein Folding Protocols. Totowa, NJ: Humana Press. pp. 115–138.
98. Meer, B.W.V.D., G. III Coker, and S.Y.S. Chen. 1994. Resonance Energy Transfer: Theory and Data. New York Weinheim: Vch Pub.
99. Klose, D., A. Holla, C. Gmeiner, D. Nettels, I. Ritsch, N. Bross, M. Yulikov, F.H.-T. Allain, B. Schuler, and G. Jeschke. 2021. Resolving distance variations by single-molecule FRET and EPR spectroscopy using rotamer libraries. *Biophysical Journal*. 120:4842–4858.



100. Zhao, H., P.H. Brown, and P. Schuck. 2011. On the Distribution of Protein Refractive Index Increments. *Biophysical Journal*. 100:2309–2317.
101. Barer, R., and S. Tkaczyk. 1954. Refractive Index of Concentrated Protein Solutions. *Nature*. 173:821–822.
102. Zheng, W., G.H. Zerze, A. Borgia, J. Mittal, B. Schuler, and R.B. Best. 2018. Inferring properties of disordered chains from FRET transfer efficiencies. *J. Chem. Phys.* 148:123329.
103. Aznauryan, M., L. Delgado, A. Soranno, D. Nettels, J. Huang, A.M. Labhardt, S. Grzesiek, and B. Schuler. 2016. Comprehensive structural and dynamical view of an unfolded protein from the combination of single-molecule FRET, NMR, and SAXS. *Proceedings of the National Academy of Sciences*. 113:E5389–E5398.
104. Dertinger, T., V. Pacheco, I. von der Hocht, R. Hartmann, I. Gregor, and J. Enderlein. 2007. Two-Focus Fluorescence Correlation Spectroscopy: A New Tool for Accurate and Absolute Diffusion Measurements. *ChemPhysChem*. 8:433–443.
105. Tinevez, J.-Y., N. Perry, J. Schindelin, G.M. Hoopes, G.D. Reynolds, E. Laplantine, S.Y. Bednarek, S.L. Shorte, and K.W. Eliceiri. 2017. TrackMate: An open and extensible platform for single-particle tracking. *Methods*. 115:80–90.
106. Fan, T.-H., J.K.G. Dhont, and R. Tuinier. 2007. Motion of a sphere through a polymer solution. *Phys. Rev. E*. 75:011803.
107. Tuinier, R., J.K.G. Dhont, and T.-H. Fan. 2006. How depletion affects sphere motion through solutions containing macromolecules. *EPL*. 75:929.
108. Muthukumar, M. 2023. *Physics of Charged Macromolecules: Synthetic and Biological Systems*. Cambridge: Cambridge University Press.
109. Hofmann, H., A. Soranno, A. Borgia, K. Gast, D. Nettels, and B. Schuler. 2012. Polymer scaling laws of unfolded and intrinsically disordered proteins quantified with single-molecule spectroscopy. *PNAS*. 109:16155–16160.
110. Soranno, A., B. Buchli, D. Nettels, R.R. Cheng, S. Müller-Späth, S.H. Pfeil, A. Hoffmann, E.A. Lipman, D.E. Makarov, and B. Schuler. 2012. Quantifying internal friction in unfolded and intrinsically disordered proteins with single-molecule spectroscopy. *PNAS*. 109:17800–17806.
111. Gopich, I.V., D. Nettels, B. Schuler, and A. Szabo. 2009. Protein dynamics from single-molecule fluorescence intensity correlation functions. *The Journal of Chemical Physics*. 131:095102.
112. Zimm, B.H. 1956. Dynamics of Polymer Molecules in Dilute Solution: Viscoelasticity, Flow Birefringence and Dielectric Loss. *The Journal of Chemical Physics*. 24:269–278.
113. Makarov, D.E. 2010. Spatiotemporal correlations in denatured proteins: The dependence of fluorescence resonance energy transfer (FRET)-derived protein reconfiguration times on the location of the FRET probes. *The Journal of Chemical Physics*. 132:035104.
114. Best, R.B., W. Zheng, and J. Mittal. 2014. Balanced Protein–Water Interactions Improve Properties of Disordered Proteins and Non-Specific Protein Association. *J. Chem. Theory Comput.* 10:5113–5124.
115. Lindorff-Larsen, K., S. Piana, K. Palmo, P. Maragakis, J.L. Klepeis, R.O. Dror, and D.E. Shaw. 2010. Improved side-chain torsion potentials for the Amber ff99SB protein force field. *Proteins: Structure, Function, and Bioinformatics*. 78:1950–1958.
116. Abascal, J.L.F., and C. Vega. 2005. A general purpose model for the condensed phases of water: TIP4P/2005. *The Journal of Chemical Physics*. 123:234505.
117. Luo, Y., and B. Roux. 2010. Simulation of Osmotic Pressure in Concentrated Aqueous Salt Solutions. *J. Phys. Chem. Lett.* 1:183–189.
118. Bussi, G., D. Donadio, and M. Parrinello. 2007. Canonical sampling through velocity rescaling. *The Journal of Chemical Physics*. 126:014101.
119. Parrinello, M., and A. Rahman. 1981. Polymorphic transitions in single crystals: A new molecular dynamics method. *Journal of Applied Physics*. 52:7182–7190.
120. Darden, T., D. York, and L. Pedersen. 1993. Particle mesh Ewald: An N·log(N) method for Ewald sums in large systems. *The Journal of Chemical Physics*. 98:10089–10092.
121. Hess, B., H. Bekker, H.J.C. Berendsen, and J.G.E.M. Fraaije. 1997. LINCS: A linear constraint solver for molecular simulations. *Journal of Computational Chemistry*. 18:1463–1472.
122. Abraham, M.J., T. Murtola, R. Schulz, S. Páll, J.C. Smith, B. Hess, and E. Lindahl. 2015. GROMACS: High performance molecular simulations through multi-level parallelism from laptops to supercomputers. *SoftwareX*. 1:19–25.
123. Karanicolas, J., and C.L. Brooks III. 2002. The origins of asymmetry in the folding transition states of protein L and protein G. *Protein Science*. 11:2351–2361.
124. Rotkiewicz, P., and J. Skolnick. 2008. Fast procedure for reconstruction of full-atom protein models from reduced representations. *Journal of Computational Chemistry*. 29:1460–1465.
125. Vitalis, A., and R.V. Pappu. 2009. ABSINTH: A new continuum solvation model for simulations of polypeptides in aqueous solutions. *Journal of Computational Chemistry*. 30:673–699.
126. Hummer, G. 2005. Position-dependent diffusion coefficients and free energies from Bayesian analysis of equilibrium and replica molecular dynamics simulations. *New J. Phys.* 7:34.

127. Best, R.B., and G. Hummer. 2010. Coordinate-dependent diffusion in protein folding. *Proceedings of the National Academy of Sciences*. 107:1088–1093.
128. Bicout, D.J., and A. Szabo. 1998. Electron transfer reaction dynamics in non-Debye solvents. *The Journal of Chemical Physics*. 109:2325–2338.
129. 2007. Numerical recipes: the art of scientific computing. 3rd ed. Cambridge, UK ; New York: Cambridge University Press.
130. Buchete, N.-V., and G. Hummer. 2008. Coarse Master Equations for Peptide Folding Dynamics. *J. Phys. Chem. B*. 112:6057–6069.
131. Zerze, G.H., J. Mittal, and R.B. Best. 2016. Diffusive Dynamics of Contact Formation in Disordered Polypeptides. *Phys. Rev. Lett.* 116:068102.
132. Best, R.B., G. Hummer, and W.A. Eaton. 2013. Native contacts determine protein folding mechanisms in atomistic simulations. *Proceedings of the National Academy of Sciences*. 110:17874–17879.
133. Qamar, S., G. Wang, S.J. Randle, F.S. Ruggeri, J.A. Varela, J.Q. Lin, E.C. Phillips, A. Miyashita, D. Williams, F. Ströhl, W. Meadows, R. Ferry, V.J. Dardov, G.G. Tartaglia, L.A. Farrer, G.S.K. Schierle, C.F. Kaminski, C.E. Holt, P.E. Fraser, G. Schmitt-Ulms, D. Klenerman, T. Knowles, M. Vendruscolo, and P.S. George-Hyslop. 2018. FUS Phase Separation Is Modulated by a Molecular Chaperone and Methylation of Arginine Cation- $\pi$  Interactions. *Cell*. 173:720-734.e15.
134. Vernon, R.M., P.A. Chong, B. Tsang, T.H. Kim, A. Bah, P. Farber, H. Lin, and J.D. Forman-Kay. 2018. Pi-Pi contacts are an overlooked protein feature relevant to phase separation. *eLife*. 7:e31486.
135. Boeynaems, S., M. De Decker, P. Tompa, and L. Van Den Bosch. 2017. Arginine-rich Peptides Can Actively Mediate Liquid-liquid Phase Separation. *Bio Protoc*. 7:e2525.
136. Staropoli, M., M. Kruteva, J. Allgaier, A. Wischnewski, and W. Pyckhout-Hintzen. 2020. Supramolecular Dimerization in a Polymer Melt from Small-Angle X-ray Scattering and Rheology: A Miscible Model System. *Polymers*. 12:880.